

¹
² Susceptible host dynamics explain pathogen resilience to
³ perturbations

⁴
⁵ Sang Woo Park, . . . , Bryan T. Grenfell, Sarah Cobey

⁶ Abstract

⁷ A major priority for epidemiological research in the time of anthropogenic change
⁸ is understanding how infectious disease dynamics respond to perturbations. Inter-
⁹ ventions to slow the spread of SARS-CoV-2 significantly disrupted the transmission
¹⁰ of other human pathogens. As interventions lifted, whether and when respiratory
¹¹ pathogens would eventually return to their pre-pandemic dynamics remains to be
¹² answered. Here, we present a framework for estimating pathogen resilience based
¹³ on how fast epidemic patterns return to their pre-pandemic, endemic dynamics and
¹⁴ analyze time series data from Hong Kong, Canada, Korea, and the US from the re-
¹⁵ sulting framework. By quantifying the resilience of common respiratory pathogens,
¹⁶ we are able to predict when each pathogen will eventually return to its pre-pandemic,
¹⁷ endemic dynamics. Our predictions about whether each pathogen should have al-
¹⁸ ready returned to its pre-pandemic dynamics closely match the observed patterns of
¹⁹ deviations (or lack thereof) from its pre-pandemic dynamics. Discrepancies between
²⁰ predicted and observed dynamics indicate the long-term impact of pandemic per-
²¹ turbations, suggesting a possibility that some pathogens may have converged to a
²² different endemic cycle. Finally, we show that the replenishment rate of the suscep-
²³ tible pool is a key determinant of pathogen resilience, which in turn determines the
²⁴ sensitivity of a system to stochastic perturbations. Overall, our analysis highlights
²⁵ the persistent nature of common respiratory pathogens.

26 Non-pharmaceutical interventions to slow the spread of SARS-CoV-2 disrupted
 27 the transmission of other human respiratory pathogens, adding uncertainties to their
 28 future epidemic dynamics and the overall public health burden [1]. As interventions
 29 lifted, large heterogeneities in outbreak dynamics were observed across different
 30 pathogens in different countries, with some pathogens exhibiting earlier resur-
 31 gences than others [2, 3, 4]. Heterogeneities in the overall reduction in transmission
 32 and the timing of re-emergence likely reflect differences in intervention patterns,
 33 pathogen characteristics, immigration/importation from other countries, and pre-
 34 pandemic pathogen dynamics [5]. Therefore, comparing the differential impact of
 35 the pandemic perturbations across pathogens can provide unique opportunities to
 36 learn about underlying pathogen characteristics, such as their transmissibility or
 37 duration of immunity, from heterogeneities in re-emergence patterns [6].

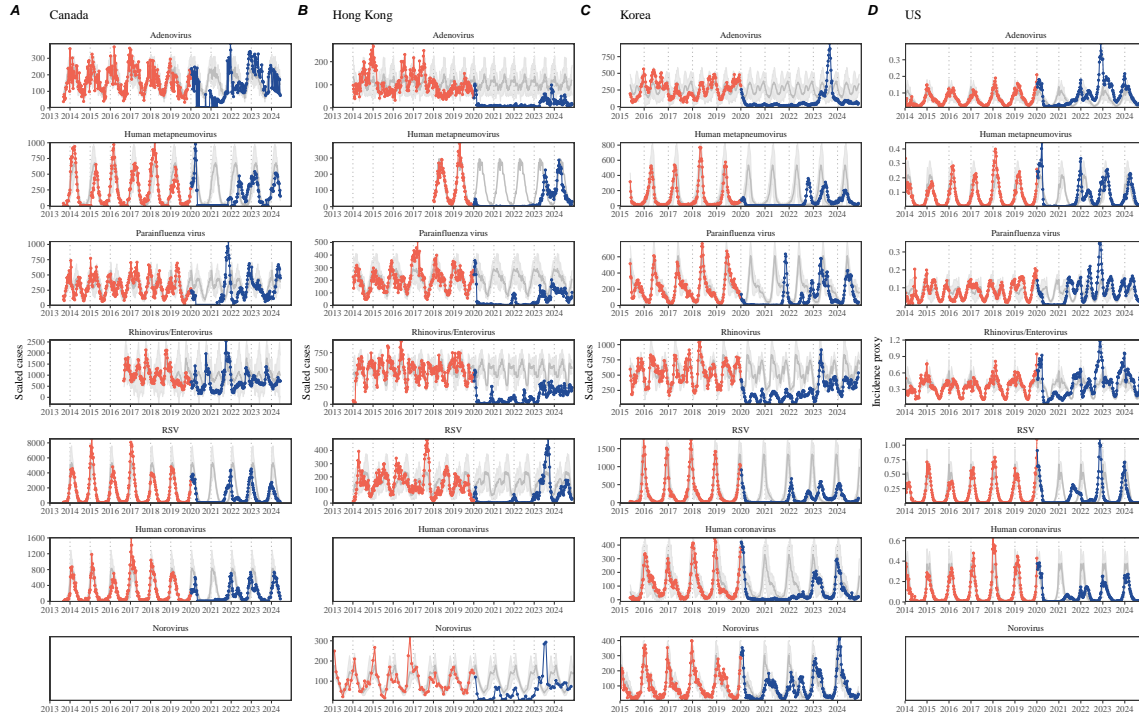


Figure 1: Observed heterogeneity in responses to pandemic perturbations across respiratory pathogens and norovirus in (A) Canada, (B) Hong Kong, (C) Korea, and (D) US. Red points and lines represent data before 2020. Blue points and lines represent data since 2020. Gray lines and shaded regions represent the mean seasonal patterns and corresponding 95% confidence intervals around the mean. Mean seasonal patterns were calculated by aggregating cases before 2020 into 52 weekly bins and taking the average in each week. Cases were scaled to account for changes in testing patterns (Materials and Methods).

38 Even though more than five years have passed since the emergence of SARS-CoV-
 39 2, we still observe persistent changes in pathogen dynamics following the pandemic

40 perturbations. For example, compared to pre-pandemic, seasonal patterns, human
41 metapneumovirus in Korea seem to circulate at lower levels, whereas RSV in Ko-
42 rea seems to exhibit different seasonality (Figure 1). These observations suggest a
43 possibility for a fundamental change in pathogen dynamics following the pandemic
44 perturbations, which can be driven by a permanent shift in either human behavior
45 or population-level immunity [7, 8]. The possibility of a long-lasting impact of the
46 pandemic perturbations poses an important question for future infectious disease
47 dynamics: can we predict whether and when other respiratory pathogens will even-
48 tually return to their pre-pandemic dynamics? *[SWP: You suggested: I would say
49 something about the dynamics of these pathogens not being well understood, but
50 I've since rewritten the most of intro and I'm not sure where I would fit this. If you
51 have any suggestions, let me know...]*

52 So far, the majority of epidemiological analyses of respiratory pathogens in the
53 context of the pandemic perturbations have focused on characterizing the timing of
54 rebound [1, 9, 5]. Instead, we seek to characterize how fast a pathogen returns to its
55 pre-pandemic dynamics. These two concepts have subtle but important differences:
56 for example, it took more than 3 years for human metapneumovirus to rebound in
57 Hong Kong but the observed epidemic patterns in 2024 are similar to pre-pandemic
58 seasonal means, suggesting a rapid return to pre-pandemic dynamics following a
59 perturbation (Figure 1). Measuring this rate of return is particularly useful because
60 it allows us to quantify the ecological resilience of a host-pathogen system [10, 11,
61 12, 13].

62 In this study, we lay out theoretical and statistical approaches to characterizing
63 the resilience of a host-pathogen system based on how fast the system recovers from
64 perturbation. We begin by laying out a few representative scenarios that capture
65 the potential impact of pandemic perturbations on endemic pathogen dynamics and
66 illustrate how resilience can be measured by comparing the pre- and post-pandemic
67 dynamics of susceptible and infected hosts. In practice, information on susceptible
68 hosts is often unavailable, making this theoretical approach infeasible. Instead, we
69 utilize a mathematical technique to reconstruct empirical attractors from the data
70 [14], which allows us to measure the rate at which the host-pathogen system ap-
71 proaches this empirical attractor after a perturbation; this rate corresponds to the
72 resilience of the host-pathogen system. We use this method to analyze pathogen
73 surveillance data for respiratory and non-respiratory pathogens from Canada, Hong
74 Kong, Korea, and the US. Finally, we show that susceptible host dynamics explain
75 variation in pathogen resilience and further link pathogen resilience to responses to
76 perturbations caused by demographic stochasticity, thereby providing a direct link
77 between pathogen resilience and persistence.

78 Conceptual introduction to pathogen resilience

79 In classical ecological literature, the resilience of an ecological system is measured by
80 the rate at which the system returns to its reference state following a perturbation
81 [10, 11, 12, 13]. This rate corresponds to the largest real part of the eigenvalues of
82 the linearized system near equilibrium—here, we refer to this value as the *intrinsic*
83 resilience of the system, which represents the expected rate of return from perturbed
84 states. In practice, we rarely know the true model describing population-level dy-
85 namics of common respiratory pathogens, limiting our ability to infer the intrinsic
86 resilience of a system. Instead, we can still measure the *empirical* resilience of a
87 host-pathogen system by looking at how fast the system returns to the pre-pandemic,
88 endemic dynamics after pandemic perturbations are lifted.

89 As an example, we begin with a simple Susceptible-Infected-Recovered-Susceptible
90 (SIRS) model with seasonally forced transmission and demography (i.e., birth and
91 death). The SIRS model is the simplest model that allows for the waning of im-
92 munity and is commonly used for modeling the dynamics of respiratory pathogens
93 [15]. First, consider a pandemic perturbation that reduces transmission by 50% for 6
94 months starting in 2020, which causes epidemic patterns to deviate from their origi-
95 nal stable annual cycle for a short period of time and eventually come back (Figure
96 2A). To measure the resilience of this system empirically, we first need to be able to
97 measure the distance from its pre-pandemic attractor. There are many ways we can
98 measure the distance from the attractor, but for illustrative purposes, we choose one
99 of the most parsimonious approaches: that is, we look at how the susceptible (S) and
100 infected (I) populations change over time and measure the distance on the SI phase
101 plane (Figure 2B). In this simple case, the locally estimated scatterplot smoothing
102 (LOESS) fit indicates that the distance from the attractor decreases exponentially
103 (linearly on a log scale) on average (Figure 2C). Furthermore, the overall rate of re-
104 turn approximates the intrinsic resilience of the seasonally unforced system (Figure
105 2C).

106 Alternatively, pandemic perturbations can have a lasting impact on the pathogen
107 dynamics; as an example, we consider a scenario in which a 10% reduction in trans-
108 mission persists even after the major pandemic perturbations are lifted (Figure 2D–
109 F). In such cases in practice, we cannot know whether the pathogen will return to
110 its original cycle or a different cycle until many years have passed, and we cannot
111 measure the distance to the new unknown attractor that the system might eventu-
112 ally approach. Nonetheless, we can still measure the distance from the pre-pandemic
113 attractor and ask how the distance changes over time (Figure 2E). The LOESS fit
114 suggests that the distance from the pre-pandemic attractor will initially decrease ex-
115 ponentially on average (equivalently, linearly on a log scale) and eventually plateau
116 (Figure 2F). Here, a permanent 10% reduction in transmission rate slows the system,
117 which causes the distance from the pre-pandemic attractor initially to decrease at a
118 slower rate (Figure 2F) than it would have otherwise (Figure 2C) before plateauing
119 at a fixed distance between the two attractors. This example shows that resilience

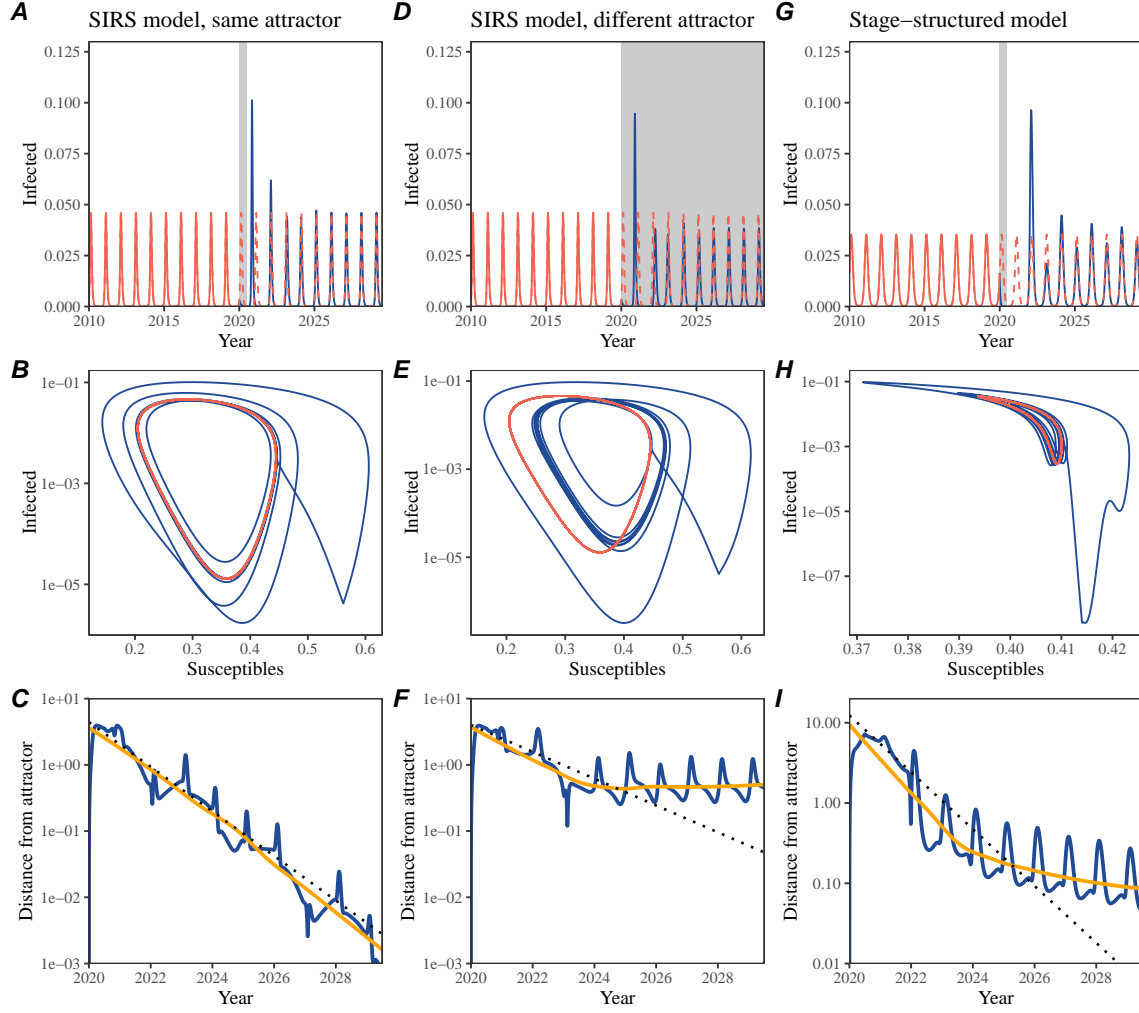


Figure 2: A simple method to measure pathogen resilience following pandemic perturbations across different scenarios. (A, D, G) Simulated epidemic trajectories across various models. Red and blue solid lines represent epidemic dynamics before and after pandemic perturbations are introduced, respectively. Red dashed lines represent counterfactual epidemic dynamics in the absence of perturbations. Gray regions indicate the duration of perturbations. (B, E, H) Phase plane representation of the time series in panels A, D, and G alongside the corresponding susceptible host dynamics. Red and blue solid lines represent epidemic trajectories on an SI phase plane before and after perturbations are introduced, respectively. (C, F, I) Changes in logged distance from the attractor over time. Blue lines represent the logged distance from the attractor. Orange lines represent the locally estimated scatterplot smoothing (LOESS) fits to the logged distance from the attractor. Dotted lines show the intrinsic resilience of the seasonally unforced system.

is not necessarily an intrinsic property of a specific pathogen. Instead, pathogen re-

121 resilience is a property of a specific attractor that a host-pathogen system approaches,
122 which depends on both pathogen and host characteristics.

123 Finally, transient phenomena can further complicate the picture (Figure 2G–I).
124 For example, a stage-structured model initially exhibits a stable annual cycle, but
125 perturbations from a 10% reduction in transmission for 6 months cause the epidemic
126 to shift to biennial cycles (Figure 2G). The system eventually approaches the original
127 pre-pandemic attractor (Figure 2H), suggesting that this biennial cycle is a transient
128 phenomenon. The LOESS fit indicates that the distance from the attractor initially
129 decreases exponentially at a rate that is consistent with the intrinsic resilience of
130 the seasonally unforced stage-structured system, but the rate of decrease decelerates
131 with the damped oscillations (Figure 2I). This behavior is also referred to as a ghost
132 attractor, which causes long transient dynamics and slow transitions [16]. Strong
133 seasonal forcing in transmission can also lead to transient phenomena for a simple
134 SIRS model, causing a slow return to pre-perturbation dynamics (Supplementary
135 Figure S1).

136 This empirical approach allows us to measure the resilience of a two-strain host-
137 pathogen system even when we have incomplete observation of the infection dynam-
138 ics. Simulations from a simple two-strain system illustrate that separate analyses of
139 individual strain dynamics (e.g., RSV A vs B) and a joint analysis of total infections
140 (e.g., total RSV infections) yield identical resilience estimates (Supplementary Fig-
141 ure S2, 3). This is expected because the dynamics of two strains (or two pathogens)
142 around the attractor in a coupled system are described by the same set of eigen-
143 values and eigenvectors, meaning that both strains should exhibit identical rates of
144 returns following a perturbation. Analogous to a single system, strong seasonal forc-
145 ing in transmission can cause the system to slow down through transient phenomena
146 (Supplementary Figure S4).

147 These observations indicate three possibilities. First, we can directly estimate the
148 empirical resilience of a host-pathogen system by measuring the rate at which the
149 system approaches an attractor, provided that we have a way to quantify the distance
150 from the attractor. The empirical approach to estimating pathogen resilience is
151 particularly convenient because it does not require us to know the true underlying
152 model; estimating the intrinsic resilience from fitting misspecified models can lead
153 to biased estimates (Supplementary Figure S5). Second, resilience estimates allow
154 us to make phenomenological predictions about the dynamics of a host-pathogen
155 system following a perturbation. Assuming that the distance from the attractor will
156 decrease exponentially over time, we can obtain a ballpark estimate for when the
157 system will reach an attractor; this prediction necessarily assumes that there won't
158 be permanent changes in pathogen dynamics (Figure 2F) or a long-term transient
159 phenomenon (Figure 2I). Finally, a change in the rate of an exponential decrease in
160 the distance from the attractor can provide information about whether the system
161 has reached an alternative attractor, or a ghost attractor, that is different from the
162 original, pre-pandemic attractor. These alternative attractors may reflect continued
163 perturbations from permanent changes in transmission patterns as well as changes in

164 immune landscapes. There will be periods of time when it is difficult to tell whether
165 pathogen dynamics are still diverging from its original attractor or have begun to
166 converge to an attractor; now that several years have passed since interventions have
167 been lifted, we expect many respiratory pathogens to have had sufficient time to
168 begin returning to their post-intervention attractors.

169 Inferring pathogen resilience from real data

170 Based on these observations, we now lay out our approach to estimating pathogen
171 resilience from real data (Figure 3). We then test this approach against simulations
172 and apply it to real data.

173 So far, we focused on simple examples that assume a constant transmission re-
174 duction. However, in practice, the impact of pandemic perturbations on pathogen
175 transmission is likely more complex (Figure 3A), reflecting introduction and relax-
176 ation of various intervention strategies. In some cases, strong perturbations can even
177 lead to a local fadeout, requiring immigration from another location for epidemic re-
178 emergence. These complexities can lead to longer delays between the introduction of
179 pandemic perturbations and pathogen re-emergence as well as temporal variation in
180 outbreak sizes (Figure 3B): in this example, continued transmission reduction from
181 interventions limits the size of the first outbreak in 2021 following the emergence,
182 allowing for a larger outbreak in 2022 when interventions are further relaxed.

183 Previously, we relied on the dynamics of susceptible and infected hosts to com-
184 pute the distance from the attractor (Figure 2), but information on susceptible hosts
185 is rarely available in practice. In addition, uncertainties in case counts due to obser-
186 vation error as well as multiannual cycles in the observed epidemic dynamics (e.g.,
187 adenovirus circulation patterns in Hong Kong and Korea) add challenges to defin-
188 ing pre-pandemic attractors, which limits our ability to measure the distance from
189 the attractor. To address these challenges, we can reconstruct an empirical attrac-
190 tor by utilizing Takens' theorem [14], which states that an attractor of a nonlinear
191 multidimensional system can be mapped onto a delayed embedding (Materials and
192 Methods). For example, we can use delayed logged values of pre-pandemic cases $C(t)$
193 (Figure 3C) to reconstruct the attractor:

$$\langle \log(C(t) + 1), \log(C(t - \tau) + 1), \dots, \log(C(t - (M - 1)\tau) + 1) \rangle, \quad (1)$$

194 where the delay τ and embedding dimension M are determined based on autocor-
195 relations and false nearest neighbors, respectively [17, 18]. We can then apply the
196 same delay and embedding dimensions to the entire time series to determine the
197 position on a multi-dimensional state space (Figure 3D), which allows us to mea-
198 sure the nearest neighbor distance between the current state of the system and the
199 empirical pre-pandemic attractor (Figure 3E). In theory, we can now quantify how
200 fast this distance decreases by fitting a linear regression on a log scale, where the
201 slope of the linear regression corresponds to pathogen resilience. However, resulting

estimates of pathogen resilience can be sensitive to choices about embedding delays and dimensions; for example, using longer delays and higher dimensions tends to smooth out temporal variations in the distance from the attractor (Supplementary Figure S6).

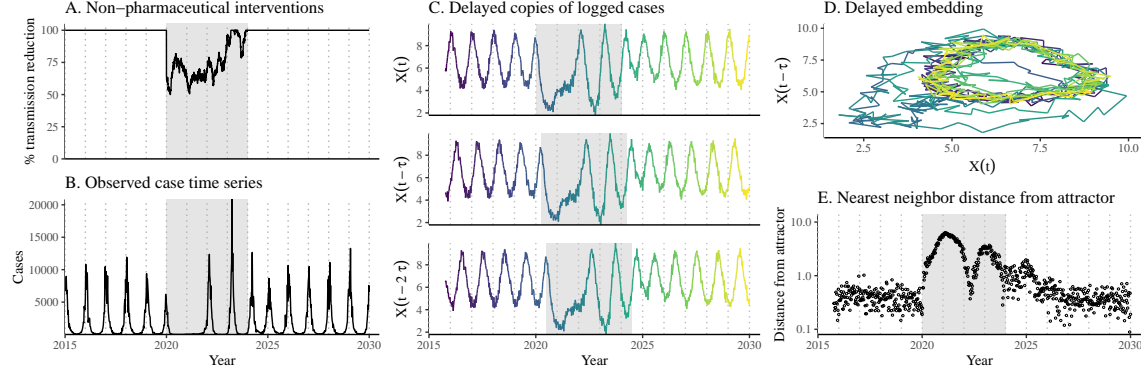


Figure 3: A schematic diagram explaining the inference of pathogen resilience from synthetic data. (A) A realistic example of simulated pandemic perturbations, represented by a relative reduction in transmission. (B) The impact of the synthetic pandemic perturbation on epidemic dynamics simulated using a SIRS model with demographic stochasticity. (C) Generating delayed copies of the logged time series allows us to obtain an embedding. (D) Two dimensional representation of an embedding. (E) Delayed embedding allows us to calculate the nearest neighbor distance from the empirical attractor, which is determined based on the pre-pandemic time series. This distance time series can be used to infer pathogen resilience after choosing an appropriate window for linear regression.

Complex changes in the distance from the attractor suggest that estimating pathogen resilience from linear regression will be particularly sensitive to our choice of fitting windows for the regression (Figure 3E). Therefore, before we tried estimating resilience from real data, we explored an automated window selection criterion for linear regression and test it against randomized, stochastic simulations across a wide range of realistic pandemic perturbation shapes; in doing so, we also explored optimal choices for embedding dimensions and evaluated our choices for fitting window parameters and embedding dimensions by quantifying correlation coefficients between the estimated resilience and the intrinsic resilience of a seasonally unforced system (Materials and Methods). Overall, we find large variation in estimation performances with correlation coefficient ranging from 0.21 to 0.61 (Supplementary Figure S7). In almost all cases, the automated window selection approach outperformed a naive approach that uses the entire time series, starting from the peak distance (Supplementary Figure S7).

Based on the best performing window selection criteria and embedding dimension, we applied this approach to pathogen surveillance data presented in Figure 1 (Materials and Methods). For each time series, we applied Takens' theorem in-

223 dependently to reconstruct the empirical attractor and obtained the corresponding
224 time series of distances from attractors (Supplementary Figure S8). Then, we use
225 the automated window selection criterion to fit a linear regression and estimate the
226 empirical resilience for each pathogen in each country (Supplementary Figure S8);
227 the window selection criterion gave poor regression window for three cases (norovirus
228 in Hong Kong and Korea and Rhinovirus/Enterovirus in the US), leading to unreal-
229 istically low resilience estimates, and so we used ad-hoc regression windows instead
230 (Supplementary Figure S9; Materials and Methods).

231 For all pathogens we consider, resilience estimates fall between 0.4/year and
232 1.8/year (Figure 4A). We estimate the mean resilience of common respiratory pathogens
233 to be 0.99/year (95% CI: 0.81/year–1.18/year). As a reference, this is \approx 7.5 times
234 higher than the intrinsic resilience of pre-vaccination measles in England and Wales
235 (\approx 0.13/year). Finally, resilience estimates for norovirus are comparable to those of
236 common respiratory pathogens: 1.44/year (95%CI: 1.01/year–1.87/year) for Hong
237 Kong and 1.07/year (95%CI: 0.86/year–1.29/year) for Korea. Based on a simple
238 ANOVA test, we do not find significant differences in resilience estimates across
239 countries ($p = 0.25$) or pathogens ($p = 0.67$).

240 [SWP: You suggested “I think we probably need to spell out a bit more that
241 long-term changes in the transmission rate (or some other parameter) mean the at-
242 tractor is permanently different and the distance should remain nonzero” and I think
243 we’ve done that enough early on with current revisions so I don’t feel like we need
244 to do it again here. Let me know what you think.] Using resilience estimates, we
245 predicted when each pathogen would hypothetically return to their pre-pandemic
246 dynamics, assuming no long-term change in the attractor. Specifically, we extend
247 our linear regression fits to distance-from-attractor time series and ask when the pre-
248 dicted regression line will cross a threshold value; since we relied on nearest neighbor
249 distances, pre-pandemic distances are always greater than zero (Figure 3E), meaning
250 that we can use the mean of pre-pandemic distances as our threshold.

251 We predict that a return to pre-pandemic cycles would be imminent for most
252 pathogens (Figure 4B). In particular, we predict that 12 out of 23 pathogens should
253 have already returned before the end of 2024. For almost all pathogens that are
254 predicted to have returned already, the observed epidemic dynamics show clear con-
255 vergence towards their pre-pandemic seasonal averages, confirming our predictions
256 (Figure 4C). However, there are a few exceptions, including norovirus in Hong Kong
257 and Rhinovirus/Enterovirus in the US, where the observed epidemic dynamics in
258 2024 exhibit clear deviation from their pre-pandemic seasonal averages (Figure 4C).
259 These observations suggest a possibility that some common respiratory pathogens
260 may have converged to different attractors or are still exhibiting non-equilibrium
261 dynamics. In contrast, pathogens that are predicted to have not returned yet also
262 show clear differences from their pre-pandemic seasonal averages; as many of these
263 pathogens are predicted to return in 2025–2026, we may be able to test these pre-
264 dictions in near future (Supplementary Figure S10). Our reconstructions of distance
265 time series and estimates of pathogen resilience and expected return time are gener-

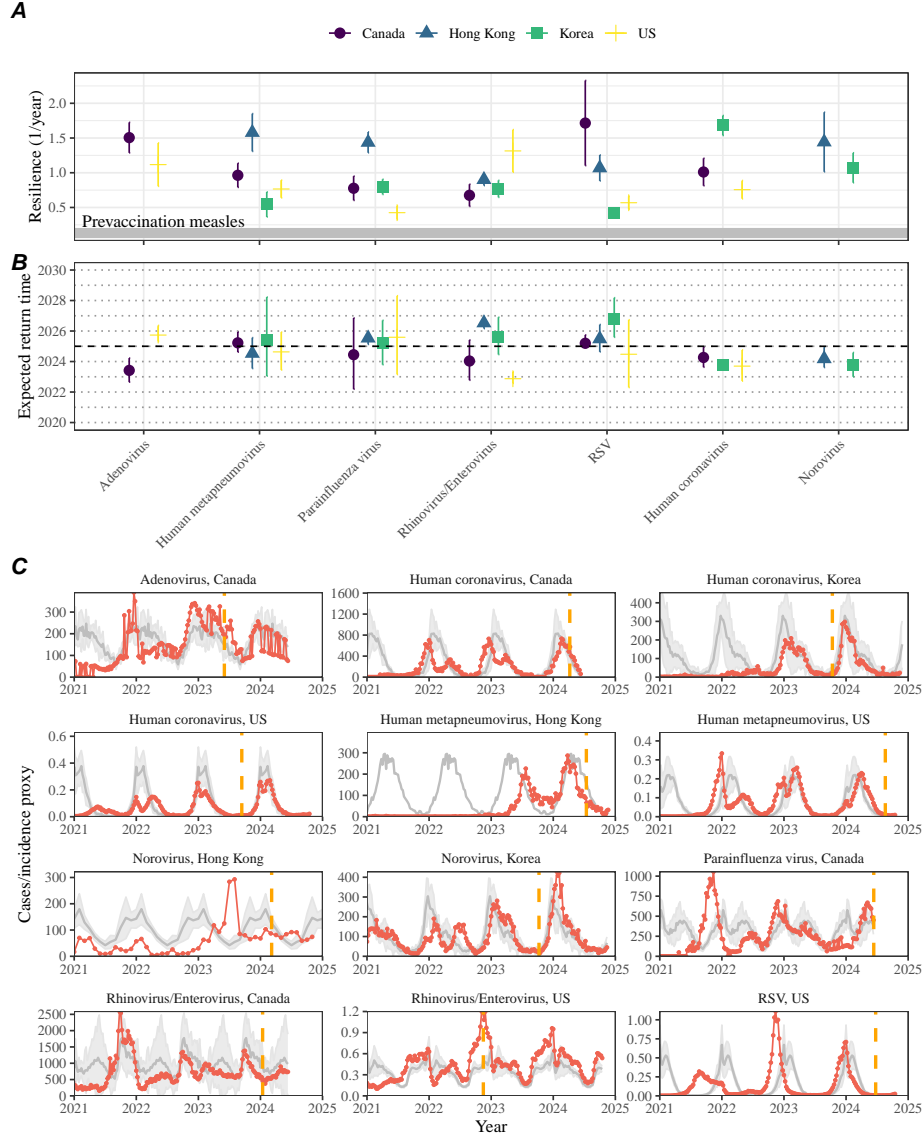


Figure 4: Summary of resilience estimates and predictions for return time. (A) Estimated pathogen resilience. The gray horizontal line represents the intrinsic resilience of pre-vaccination measles dynamics. (B) Predicted timing of when each pathogen will return to their pre-pandemic cycles. The dashed line in panel B indicates the end of 2024 (current observation time). Error bars represent 95% confidence intervals. (C) Observed dynamics for pathogen that are predicted to have returned before the end of 2024. Red points and lines represent data before 2020. Gray lines and shaded regions represent the mean seasonal patterns and corresponding 95% confidence intervals around the mean, previously shown in Figure 1. Orange vertical lines represent the predicted timing of return.

266 ally robust to choices of embedding dimensions (Supplementary Figure S11–12).

267 **Susceptible host dynamics explain variation in pathogen
268 resilience**

269 So far, we focused on quantifying pathogen resilience from the observed patterns
270 of pathogen re-emergence following pandemic perturbations. But what factors de-
271 termine how resilient a host-pathogen system is? Here, we use the SIRS model to
272 show that susceptible host dynamics are the key determinants of pathogen resilience.
273 To do so, we vary the basic reproduction number \mathcal{R}_0 , which represents the average
274 number of secondary infections caused by a newly infected individual in a fully sus-
275 ceptible population, and the duration of immunity and compute intrinsic resilience
276 for each parameter.

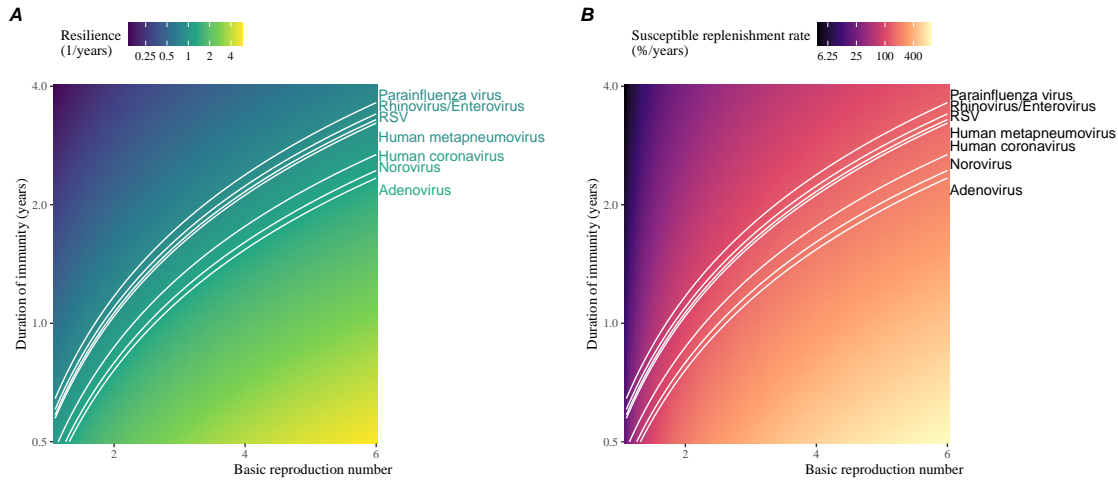


Figure 5: **Linking pathogen resilience to epidemiological parameters and susceptible host dynamics.** (A) The heat map represents intrinsic resilience as a function of the basic reproduction number \mathcal{R}_0 and the duration of immunity. (B) The heat map represents per-capita susceptible replenishment rate as a function of the basic reproduction number \mathcal{R}_0 and the duration of immunity. The standard SIRS model is used to compute intrinsic resilience and per-capita susceptible replenishment rate. Lines correspond to a set of parameters that are consistent with mean resilience estimates for each pathogen. Pathogens are ranked based on their mean resilience estimates, averaged across different countries.

277 We find an increase in \mathcal{R}_0 and a decrease in duration of immunity correspond
278 to an increase in pathogen resilience (Figure 5A). These variations can be under-
279 stood in terms of the susceptible host dynamics, where faster per-capita susceptible
280 replenishment rate causes the system to be more resilient (Figure 5B). This rate can

281 be expressed as a ratio between absolute rate at which new susceptibles enter the
282 population and the equilibrium number of susceptible individuals in the population,
283 \bar{S} . Therefore, both higher \mathcal{R}_0 and shorter duration of immunity can drive faster
284 per-capita susceptible replenishment rate (Figure 5B), especially because higher \mathcal{R}_0
285 leads to lower \bar{S} .

286 We can also rank different pathogens based on the average values of empirical
287 resilience computed previously, which allows us to determine a set of parameters that
288 are consistent with the estimated resilience (Figure 5A). Across all pathogens we
289 consider, except for bocavirus and norovirus, we estimate that the average duration
290 of immunity is likely to be short (< 4 years) across a plausible range of \mathcal{R}_0 (< 6).
291 These rankings further allow us to map each pathogen onto a set of SIRS parameters
292 that are consistent with its empirical resilience (Figure 5A) and obtain a plausible
293 range of susceptible replenishment rates for each pathogen (Figure 5B). However, we
294 note that there is no one-to-one correspondence between susceptible replenishment
295 rates and pathogen resilience, leading to a wide uncertainty in the estimates for
296 susceptible replenishment rates (Figure 5B).

297 **Pathogen resilience determines sensitivity to stochastic perturbations**

298

299 Beyond the pandemic perturbations, we expect host-pathogen systems to experience
300 continued perturbations of varying degrees from changes in epidemiological conditions,
301 such as human behavior, climate, and viral evolution. These perturbations
302 can also arise from demographic stochasticity, which is inherent to any ecological
303 systems. Here, we use a seasonally unforced SIRS model with birth/death to explore
304 how resilience of a host-pathogen system determines the sensitivity to perturbations
305 caused by demographic stochasticity (Materials and Methods).

306 We find that resilience of a host-pathogen system determines the amount of deviation
307 from the deterministic trajectory caused by demographic stochasticity, with less
308 resilient systems experiencing larger deviations (Figure 6). Notably, less resilience
309 systems also exhibit slower epidemic cycles; the periodicity of this epidemic cycle
310 matches those predicted by the intrinsic periodicity of the system (Supplementary
311 Figure S13). These conclusions are robust for the seasonally forced SIRS model
312 (Supplementary Figure S14),

313 **Discussion**

314 The pandemic interventions have caused major disruptions to circulation patterns of
315 both respiratory and non-respiratory pathogens, adding challenges to predicting their
316 future dynamics [1, 2, 3, 4]. However, these perturbations offer large-scale natural
317 experiments for understanding how different pathogens respond to perturbations. In

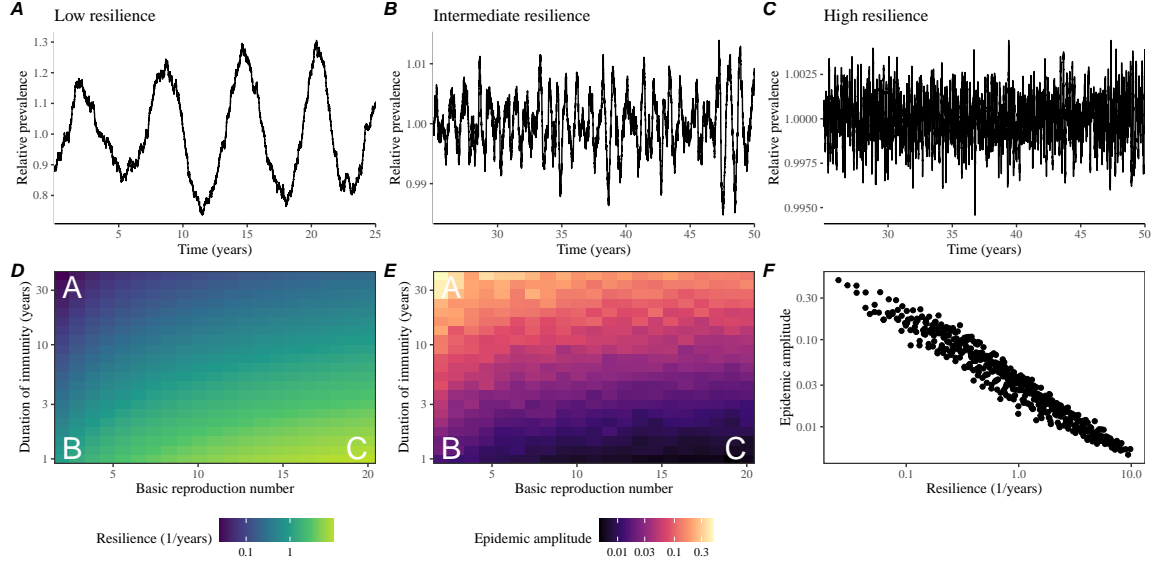


Figure 6: Linking resilience of a host-pathogen system to its sensitivity to stochastic perturbations. (A–C) Epidemic trajectories of a stochastic SIRS model across three different resilience values: low, intermediate, and high. The relative prevalence was calculated by dividing infection prevalence by its mean value. (D) The heat map represents the intrinsic resilience of a system as a function of the basic reproduction number \mathcal{R}_0 and the duration of immunity. (E) The heat map represents the epidemic amplitude as a function of the basic reproduction number \mathcal{R}_0 and the duration of immunity. The epidemic amplitude corresponds to $(\max I - \min I)/(2\bar{I})$, where \bar{I} represents the mean prevalence. (F) The relationship between pathogen resilience and epidemic amplitude.

318 this study, we showed that pathogen re-emergence patterns following pandemic per-
 319 turbations can be characterized through the lens of ecological resilience. We showed
 320 that variation in pathogen resilience can be explained by the differences in suscepti-
 321 ble host dynamics, where faster replenishment of the susceptible pool corresponds to
 322 a more resilient host-pathogen system. Finally, we showed that pathogen resilience
 323 also determines the sensitivity to stochastic perturbations.

324 We analyzed case time series of common respiratory infections and norovirus
 325 infections from Canada, Hong Kong, Korea, and the US to estimate their resilience.
 326 Overall, we estimated the resilience of these pathogens to range from 0.4/year to
 327 1.8/year, which is 3–14 times more resilient than prevaccination measles. These
 328 resilience estimates indicate that common respiratory pathogens and norovirus likely
 329 exhibit faster susceptible replenishment and are therefore more persistent, indicating
 330 potential challenges in controlling these pathogens.

331 Based on our resilience estimates, we made phenomenological predictions about
 332 when each pathogen will return to their endemic cycles. For the most part, we

333 accurately predicted which pathogens should have already returned before the end
334 of 2024. However, there were few exceptions (i.e., norovirus in Hong Kong and
335 rhinovirus/enterovirus in the US), suggesting a possibility that these may have con-
336 verged to different endemic cycles compared to their pre-pandemic epidemic patterns.
337 These changes may reflect changes in surveillance or actual shift in the dynamics,
338 caused by permanent changes in behavior or population-level immunity. While it may
339 seem unlikely that permanent changes in behavior would only affect a few pathogens
340 and not others, we cannot rule out this possibility given heterogeneity in the age of
341 infection across different respiratory pathogens [19, 20]. Differences in the mode of
342 transmission between respiratory vs gastrointestinal pathogens may also contribute
343 to the differences in responses to pandemic perturbations. However, it is unclear
344 why norovirus dynamics in Korea seemed to have returned, whereas those in Hong
345 Kong have not.

346 For almost half of the pathogens we considered, we predicted that their return
347 to original epidemic patterns is imminent. We will need a few more years of data
348 to test whether these pathogens will eventually return to their original dynamics
349 or eventually converge to a different attractor. Overall, these observations echo
350 earlier studies that highlighted the long-lasting impact of pandemic perturbations
351 [8, 21, 22, 4].

352 We showed that susceptible host dynamics shape pathogen resilience, where faster
353 replenishment of the susceptible population causes the pathogen to be more resilient.
354 For simplicity, we focus on waning immunity and birth as the main drivers of the
355 susceptible host dynamics but other mechanisms can also contribute to the replen-
356 ishment of the susceptible population. In particular, pathogen evolution, especially
357 the emergence of antigenically novel strains, can cause effective waning of immunity
358 in the population; therefore, we hypothesize that faster rates of antigenic evolution
359 can also cause a pathogen to be more resilient. Future studies should explore the
360 relationship between the rate of evolution and resilience for antigenically evolving
361 pathogens.

362 Quantifying pathogen resilience also offers novel approaches to validating population-
363 level epidemiological models. So far, most of model validation in infectious disease
364 ecology is based on the ability of a model to reproduce the observed epidemic dy-
365 namics and to predict future dynamics [23, 24, 25, 26, 27]. However, many models
366 can perform similarly under these criteria. For example, two major RSV models
367 have been proposed to explain biennial epidemic patterns: (1) a stage- and age-
368 structured model that allows disease severity to vary with number of past infections
369 and age of infection [25] and (2) a pathogen-interaction model that accounts for cross
370 immunity between RSV and human metapneumovirus [24]. Since both models can
371 accurately reproduce the observed epidemic patterns, standard criteria for model
372 validation do not allow us to distinguish between these two models from population-
373 level data alone. Instead, it would be possible to measure the empirical resilience of
374 each model by simulating various perturbations and compare them to estimates of
375 empirical resilience from data, using pandemic perturbations as an opportunity.

376 There are several limitations to our work. First, we did not extensively explore
377 other approaches to reconstructing the attractor. Recent studies showed that more
378 sophisticated approaches, such as using non-uniform embedding, can provide more
379 robust reconstruction for noisy data [18]. In the context of causal inference, choices
380 about embedding can have major impact on the resulting inference [28]. Our re-
381 silience estimates are likely overly confident given a lack of uncertainties in attractor
382 reconstruction as well as the simplicity of our statistical framework. Nonetheless,
383 as illustrated in our sensitivity analyses, inferences about pathogen resilience in our
384 SIRS model appear to be robust to decisions about embedding lags and dimensions—
385 this is because tracking the rate at which the system approaches the attractor is
386 likely a much simpler problem than making inferences about causal directionality.
387 Short pre-pandemic time series also limit our ability to accurately reconstruct the
388 attractor and contribute to the crudeness of our resilience estimates; although this is
389 less likely a problem for respiratory pathogens that are strongly annual, our attrac-
390 tor reconstruction may be inaccurate for those exhibiting multi-annual cycles, such
391 as adenovirus in Hong Kong and Korea. Uncertainties in pathogen dynamics due
392 to changes in testing patterns further contribute to the curdeness of our resilience
393 estimates. Despite these limitations, our qualitative prediction that common respi-
394 ratory pathogens are more resilient than prevaccination measles is also likely to be
395 robust, given how rapid many respiratory pathogens returned to their original cycles
396 following pandemic perturbations.

397 Predicting the impact of anthropogenic changes on infectious disease dynamics
398 is a fundamental aim of infectious disease research in a rapidly changing world. Our
399 study illustrates that how a host-pathogen system responds to both small and large
400 perturbations is largely predictable through the lens of ecological resilience. In par-
401 ticular, quantifying the resilience of a host-pathogen system offers a unique insight
402 into questions about endemic pathogens' responses to pandemic perturbations, in-
403 cluding whether some pathogens will exhibit long-lasting impact from the pandemic
404 perturbation or not. More broadly, a detailed understanding of the determinants of
405 pathogen resilience can provide deeper understanding of pathogen persistence.

406 Materials and Methods

407 Data

408 We gathered time series on respiratory infections from Canada, Hong Kong, Korea,
409 and United States (US). As a reference, we also included time series data on norovirus
410 infections for available countries. In contrast to respiratory pathogens, we expect
411 gastrointestinal viruses, such as norovirus, to be differently affected by pandemic
412 perturbations.

413 Weekly time series of respiratory infection cases in Canada comes from a pub-
414 licly available website by the Respiratory Virus Detection Surveillance System, which
415 collect data from select laboratories across Canada [29]. Weekly time series of respi-

416 respiratory infection cases in Hong Kong comes from a publicly available website by the
417 Centre for Health Protection, Department of Health [30, 31]. Weekly time series of
418 acute respiratory infection cases in Korea comes from a publicly available website by
419 the Korea Disease Control and Prevention Agency [32]. Finally, weekly time series
420 of respiratory infection cases in the US were obtained from the National Respiratory
421 and Enteric Virus Surveillance System. Time series on number of tests were also
422 available in Canada, Hong Kong, and the US, but not in Korea. **[SWP: Not sure**
423 *how to cite NREVSS data because we got it by emailing them...*]

424 **Data processing**

425 For all time series, we rounded every year to 52 weeks by taking the average number
426 of cases and tests between the 52nd and 53rd week. We also rescale all time series to
427 account for changes in testing patterns, which are then used for the actual analysis.

428 For Canada, an increase in testing was observed from 2013 to 2024 (Supplementary
429 Figure S15). To account for this increase, we calculated a 2 year moving average
430 for the number of tests for each pathogen, which we used as a proxy for testing effort.
431 Then, we divided the smoothed testing patterns by the smoothed value at the final
432 week such that the testing effort has a maximum of 1. We then divided weekly cases
433 by the testing effort to obtain a scaled case time series. A similar approach was used
434 earlier for an analysis of RSV time series in the US to account for changes in testing
435 patterns [25].

436 For Hong Kong, we also applied the same scaling procedure to the time series
437 as we did for Canada. In this case, we only adjusted for testing efforts up to the
438 end of 2019 because there was a major reduction in testing for common respiratory
439 pathogens since 2020 (Supplementary Figure S16).

440 For Korea, while we did not have information on testing, the reported number
441 of respiratory infections consistently increased from 2013 to the end of 2019, which
442 we interpreted as changes in testing patterns (Supplementary Figure S17). Since
443 we did not have testing numbers, we used the weekly sum of all acute respiratory
444 viral infection cases as a proxy for testing, which were further smoothed with moving
445 averaged and scaled to have a maximum of 1. For Korea, we also only adjusted for
446 testing efforts up to the end of 2019.

447 In the US, there has been a large increase in testing against some respiratory
448 pathogens, especially RSV, which could not be corrected for through simple scaling
449 (Supplementary Figure S18). Instead, we derived an incidence proxy by multiplying
450 the test positivity with influenza-like illness positivity, which was taken from
451 <https://gis.cdc.gov/grasp/fluview/fluportaldashboard.html>. This method
452 of estimating an incidence proxy has been recently applied in the analysis of seasonal
453 coronaviruses [7] and *Mycoplasma pneumoniae* infections [4]. Detailed assumptions
454 and justifications are provided in [33].

455 **Estimating pathogen resilience**

456 In order to measure pathogen resilience from surveillance data, we first reconstructed
 457 the empirical pre-pandemic attractor of the system using Takens' embedding theorem
 458 [14]. Specifically, for a given pathogen, we took the pre-pandemic (before 2020)
 459 case time series $C(t)$ and reconstruct the attractor using delayed embedding with a
 460 uniform delay of τ and dimension M :

$$X_{\tau,m}(t) = \langle \log(C(t) + 1), \log(C(t - \tau) + 1), \dots, \log(C(t - (M-1)\tau) + 1) \rangle. \quad (2)$$

461 Here, the delay τ was determined by calculating the autocorrelation of the logged
 462 pre-pandemic time series and asking when the autocorrelation crosses 0 for the first
 463 time [18]; a typical delay for an annual outbreak is around 13 weeks.

464 Then, for a given delay τ , we determined the embedding dimension M using the
 465 false nearest neighbors approach [17, 18]. To do so, we started with an embedding
 466 dimension e and construct a set of points $A_{\tau,e} = \{X_{\tau,e}(t) | t < 2020\}$. Then, for
 467 each point $X_{\tau,e}(t)$, we determined the nearest neighbor from the set $A_{\tau,e}$, which we
 468 denote $X_{\tau,e}(t_{nn})$ for $t \neq t_{nn}$. Then, if the distance between these two points on $e+1$
 469 dimension, $D_{\tau,e+1}(t) = \|X_{\tau,e+1}(t_{nn}) - X_{\tau,e+1}(t)\|_2$, is larger than their distance on
 470 e dimension, $D_{\tau,e}(t) = \|X_{\tau,e}(t_{nn}) - X_{\tau,e}(t)\|_2$, these two points are deemed to be
 471 false nearest neighbors; specifically, we used a threshold R for the ratio between
 472 two distances $D_{\tau,e+1}(t)/D_{\tau,e}(t)$ to determine false nearest neighbors. For the main
 473 analysis, we used $R = 10$, which was chosen from a sensitivity analysis against
 474 simulated data (Supplementary Text). Once we determined the embedding lag τ
 475 and dimension M , we apply the embedding to the entire time series and calculate
 476 the nearest neighbor distance against the attractor $A_{\tau,M}$ to obtain a time series of
 477 distance from the attractor $D_{\tau,M}(t)$.

478 From a time series of distances from the attractor, we estimated pathogen re-
 479 silience by fitting a linear regression to an appropriate window. To automatically se-
 480 lect the fitting window, we began by smoothing the distance time series using locally
 481 estimated scatterplot smoothing (LOESS) to obtain $\hat{D}_{\tau,M}(t)$, where the smoothing
 482 is performed on a log scale and exponentiated afterwards. Then, we determined
 483 threshold values (T_{start} and T_{end}) for the smoothed distances and choose the fitting
 484 window based on when $\hat{D}_{\tau,M}(t)$ crosses these threshold values for the first time.
 485 These thresholds were determined by first calculating maximum distance,

$$\max \hat{D} = \max \hat{D}_{\tau,M}(t), \quad (3)$$

486 and mean pre-pandemic distance,

$$\hat{D}_{\text{mean}} = \frac{1}{N_{t<2020}} \sum_{t<2020} \hat{D}_{\tau,M}(t), \quad (4)$$

487 as a reference, and then dividing their ratios into K equal bins:

$$T_{\text{start}} = \hat{D}_{\text{mean}} \times \left(\frac{\max \hat{D}}{\hat{D}_{\text{mean}}} \right)^{(K-a)/K} \quad (5)$$

$$T_{\text{end}} = \hat{D}_{\text{mean}} \times \left(\frac{\max \hat{D}}{\hat{D}_{\text{mean}}} \right)^{a/K} \quad (6)$$

488 where a represents the truncation threshold. This allows us to discard the initial
 489 period during which the distance increases (from the introduction of intervention
 490 measures) and the final period during which the distance plateaus (as the system
 491 reaches an attractor). The fitting window is determined based on when the smoothed
 492 distance $\hat{D}_{\tau,M}(t)$ crosses these threshold values for the first time; then, we fit a
 493 linear regression to logged (unsmoothed) distances $\log D_{\tau,M}(t)$ using that window.
 494 Alongside the threshold R for the false nearest neighbors approach, we tested optimal
 495 choices for K and a values using simulations (Supplementary Text). We used $K = 19$
 496 and $a = 2$ throughout the paper based on the simulation results.

497 Mathematical modeling

498 Throughout the paper, we use a series of mathematical models to illustrate the
 499 concept of pathogen resilience and to understand the determinants of pathogen re-
 500 silience. In general, the intrinsic resilience for a given system is given by the largest
 501 real part of the eigenvalues of the linearized system at endemic equilibrium. Here, we
 502 focus on the SIRS model with demography (birth and death) and present the details
 503 of other models in Supplementary Text. The SIRS (Susceptible-Infected-Recovered-
 504 Susceptible) model is the simplest model that allows for waning of immunity, where
 505 recovered (immune) individuals are assumed to become fully susceptible after an
 506 average of $1/\delta$ time period. The dynamics of the SIRS model is described by the
 507 following set of differential equations:

$$\frac{dS}{dt} = \mu - \beta(t)SI - \mu S + \delta R \quad (7)$$

$$\frac{dI}{dt} = \beta(t)SI - (\gamma + \mu)I \quad (8)$$

$$\frac{dR}{dt} = \gamma I - (\delta + \mu)R \quad (9)$$

(10)

508 where μ represents the birth/death rate, $\beta(t)$ represents the time-varying trans-
 509 mission rate, and γ represents the recovery rate. The basic reproduction number
 510 $\mathcal{R}_0(t) = \beta(t)/(\gamma + \mu)$ is defined as the average number of secondary infections that
 511 a single infected individual would cause in a fully susceptible population at time t
 512 and measures the intrinsic transmissibility of a pathogen.

513 When we first introduced the idea of pathogen resilience (Figure 2), we imposed
 514 sinusoidal changes to the transmission rate to account for seasonal transmission:

$$\beta(t) = b_1(1 + \theta \cos(2\pi(t - \phi)))\alpha(t), \quad (11)$$

515 where b_1 represents the baseline transmission rate, θ represents the seasonal amplitude,
 516 and ϕ represents the seasonal offset term. Here, we also introduced an extra
 517 multiplicative term $\alpha(t)$ to account for the impact of pandemic perturbations, where
 518 $\alpha(t) < 1$ indicates transmission reduction. Figure 2A and 2B were generated assuming
 519 $b_1 = 3 \times (365/7 + 1/50)/\text{years}$, $\theta = 0.2$, $\phi = 0$, $\mu = 1/50/\text{years}$, $\gamma = 365/7/\text{years}$,
 520 and $\delta = 1/2/\text{years}$. In Figure 2A, we imposed a 50% transmission reduction for 6
 521 months from 2020:

$$\alpha(t) = \begin{cases} 0.5 & 2020 \leq t < 2020.5 \\ 1 & \text{otherwise} \end{cases} \quad (12)$$

522 In Figure 2B, we imposed a 50% transmission reduction for 6 months from 2020 and
 523 a permanent 10% reduction onward:

$$\alpha(t) = \begin{cases} 1 & t < 2020 \\ 0.5 & 2020 \leq t < 2020.5 \\ 0.9 & 2020.5 \leq t \end{cases} \quad (13)$$

524 In both scenarios, we simulated the SIRS model from the following initial conditions
 525 ($S(0) = 1/\mathcal{R}_0$, $I(0) = 1 \times 10^{-6}$, and $R(0) = 1 - S(0) - I(0)$) from 1900 until 2030.

526 To measure the empirical resilience of the SIRS model (Figure 2C and 2F), we
 527 computed the normalized distance between post-intervention susceptible and logged
 528 infected proportions and their corresponding unperturbed values at the same time:

$$\sqrt{\left(\frac{S(t) - S_{\text{unperturbed}}(t)}{\sigma_S}\right)^2 + \left(\frac{\log I(t) - \log I_{\text{unperturbed}}(t)}{\sigma_{\log I}}\right)^2}, \quad (14)$$

529 where σ_S and $\sigma_{\log I}$ represent the standard deviation in the unperturbed susceptible
 530 and logged infected proportions. The unperturbed values were obtained by simulating
 531 the same SIRS model without pandemic perturbations ($\alpha = 1$). We normalized
 532 the differences in susceptible and logged infected proportions to allow both quantities
 533 to equally contribute to the changes in distance from the attractor. We used logged
 534 prevalence, instead of absolute prevalence, in order to capture epidemic dynamics
 535 in deep troughs during the intervention period. In Supplementary Materials, we
 536 also compared how the degree of seasonal transmission affects empirical resilience
 537 by varying θ from 0 to 0.4; when we assumed no seasonality ($\theta = 0$), we did not
 538 normalize the distance because the standard deviation of pre-intervention dynamics
 539 are zero.

540 We used the SIRS model to understand how underlying epidemiological parameters
 541 affect pathogen resilience and link this relationship to underlying susceptible
 542 host dynamics. For the simple SIRS model without seasonal transmission ($\theta = 0$),
 543 the intrinsic resilience corresponds to

$$-\frac{\text{Re}(\lambda)}{2} = \frac{\delta + \beta I^* + \mu}{2}. \quad (15)$$

544 Here, I^* represents the prevalence at endemic equilibrium:

$$I^* = \frac{(\delta + \mu)(\beta - (\gamma + \mu))}{\beta(\delta + \gamma + \mu)}. \quad (16)$$

545 The susceptible replenishment rate is given by

$$S_{\text{replenish}} = \frac{\mu + \delta R}{S^*}, \quad (17)$$

546 where $S^* = 1/\mathcal{R}_0$ represents the equilibrium proportion of susceptible individuals.
547 We varied the basic reproduction number \mathcal{R}_0 between 1.1 to 6 and the average
548 duration of immunity $1/\delta$ between 2 to 4 years, and computed these two quantities.
549 In doing so, we fixed all other parameters: $\mu = 1/80/\text{years}$ and $\gamma = 365/7/\text{years}$.

550 Finally, we used a seasonally unforced stochastic SIRS model without demog-
551 raphy to understand how pathogen resilience affects sensitivity of the system to
552 demographic stochasticity (see Supplementary Text for the details of the stochastic
553 SIRS model). By varying the basic reproduction number \mathcal{R}_0 between 2 to 20 and
554 the average duration of immunity $1/\delta$ between 1 to 40 years, we ran the the SIRS
555 model for 100 years and computed the epidemic amplitude, which we defined as
556 $(\max I - \min I)/(2\bar{I})$. Each simulation began from the equilibrium, and we trun-
557 cated initial 25 years before computing the epidemic amplitude. In doing so, we
558 assumed $\gamma = 365/7/\text{years}$ and fixed the population size to 1 billion to prevent any
559 fadeouts. We also considered using a seasonally forced stochastic SIRS model with-
560 out demography, assuming an amplitude of seasonal forcing of 0.04; in this case,
561 we computed the relative epidemic amplitude by comparing the deterministic and
562 stochastic trajectories (Supplementary Materials).

563 Data availability

564 All data and code are stored in a publicly available GitHub repository (<https://github.com/cobeylab/return-time>).

566 Funding

567 S.W.P. is a Peter and Carmen Lucia Buck Foundation Awardee of the Life Sciences
568 Research Foundation.

569 **Supplementary Text**

570 **Resilience of a stage-structured system.**

571 In Figure 2G–I, we used a more realistic, stage-structured model to illustrate how
 572 transient phenomena can cause the system to slow down. Specifically, we used the
 573 stage-structured RSV model proposed by [25], which assumes that subsequent rein-
 574 fections cause an individual to become less susceptible and transmissible than previ-
 575 ous infections. The model dynamics can be described as follows:

$$\frac{dM}{dt} = \mu - (\omega + \mu)M \quad (S1)$$

$$\frac{dS_0}{dt} = \omega M - (\lambda(t) + \mu)S_0 \quad (S2)$$

$$\frac{dI_1}{dt} = \lambda(t)S_0 - (\gamma_1 + \mu)I_1 \quad (S3)$$

$$\frac{dS_1}{dt} = \gamma_1 I_1 - (\sigma_1 \lambda(t) + \mu)S_1 \quad (S4)$$

$$\frac{dI_2}{dt} = \sigma_1 \lambda(t)S_1 - (\gamma_2 + \mu)I_2 \quad (S5)$$

$$\frac{dS_2}{dt} = \gamma_2 I_2 - (\sigma_2 \lambda(t) + \mu)S_2 \quad (S6)$$

$$\frac{dI_3}{dt} = \sigma_2 \lambda(t)S_2 - (\gamma_3 + \mu)I_3 \quad (S7)$$

$$\frac{dS_3}{dt} = \gamma_3 I_3 - (\sigma_3 \lambda(t) + \mu)S_3 + \gamma_4 I_4 \quad (S8)$$

$$\frac{dI_4}{dt} = \sigma_3 \lambda(t)S_3 - (\gamma_4 + \mu)I_4 \quad (S9)$$

(S10)

576 where M represents the proportion of individuals who are maternally immune; S_i
 577 represents the proportion of individuals who are susceptible after i prior infections; I_i
 578 represents the proportion of individuals who are currently (re)-infected with their i -th
 579 infection; μ represents the birth and death rates; $1/\omega$ represents the mean duration
 580 of maternal immunity; $1/\gamma_i$ represents the mean duration of infection; $\lambda(t)$ represents
 581 the force of infection; and σ_i represents the reduction in susceptibility for the i -th
 582 reinfection. The force of infection is modeled using a sinusoidal function:

$$\beta(t) = b_1(1 + \theta \cos(2\pi(t - \phi)))\alpha(t) \quad (S11)$$

$$\lambda(t) = \beta(I_1 + \rho_1 I_2 + \rho_2(I_3 + I_4)), \quad (S12)$$

583 where b_1 represents the baseline transmission rate; θ represents the seasonal ampli-
 584 tude; ϕ represents the seasonal offset term; $\alpha(t)$ represents the intervention effect;
 585 and ρ_i represents the impact of immunity on transmission reduction. We used the

586 following parameters to simulate the impact of interventions on epidemic dynam-
 587 ics [25]: $b_1 = 9 \times (365/10 + 1/80)/\text{years}$, $\theta = 0.2$, $\phi = -0.1$, $\omega = 365/112/\text{years}$,
 588 $\gamma_1 = 365/10/\text{years}$, $\gamma_2 = 365/7/\text{years}$, $\gamma_3 = 365/5/\text{years}$, $\sigma_1 = 0.76$, $\sigma_2 = 0.6$,
 589 $\sigma_3 = 0.4$, $\rho_1 = 0.75$, $\rho_2 = 0.51$, and $\mu = 1/80/\text{years}$. We assumed a 50% transmis-
 590 sion reduction for 6 months from 2020:

$$\alpha(t) = \begin{cases} 0.5 & 2020 \leq t < 2020.5 \\ 1 & \text{otherwise} \end{cases} \quad (\text{S13})$$

591 The model was simulated from 1900 to 2030 using the following initial conditions:
 592 $M = 0$, $S_0 = 1/\mathcal{R}_0 - I_1$, $I_1 = 1 \times 10^{-6}$, $S_1 = 1 - 1/\mathcal{R}_0$, $I_2 = 0$, $S_2 = 0$, $I_3 = 0$,
 593 $S_3 = 0$, and $I_4 = 0$. For the phase plane analysis (Figure 2H) and distance analysis
 594 (Figure 2I), we relied on the average susceptibility,

$$\bar{S} = S_0 + \sigma_1 S_1 + \sigma_2 S_2 + \sigma_3 S_3, \quad (\text{S14})$$

595 and total prevalence,

$$I_{\text{total}} = I_1 + I_2 + I_3 + I_4. \quad (\text{S15})$$

596 These quantities were used to compute the normalized distance from the attractor,
 597 as described in the main text.

598 Resilience of a multistrain system.

599 We used a simple two-strain model to show that a multistrain host-pathogen system
 600 that is coupled through cross immunity can be described by a single resilience value.
 601 The model dynamics can be described as follows [24]:

$$\frac{dS}{dt} = \mu - \mu S - (\lambda_1 + \lambda_2)S + \rho_1 R_1 + \rho_2 R_2 \quad (\text{S16})$$

$$\frac{dI_1}{dt} = \lambda_1 S - (\gamma_1 + \mu)I_1 \quad (\text{S17})$$

$$\frac{dI_2}{dt} = \lambda_2 S - (\gamma_2 + \mu)I_2 \quad (\text{S18})$$

$$\frac{dR_1}{dt} = \gamma_1 I_1 - \lambda_2 \epsilon_{21} R_1 - \rho_1 R_1 + \rho_2 R - \mu R_1 \quad (\text{S19})$$

$$\frac{dR_2}{dt} = \gamma_2 I_2 - \lambda_1 \epsilon_{12} R_2 - \rho_2 R_2 + \rho_1 R - \mu R_2 \quad (\text{S20})$$

$$\frac{dJ_1}{dt} = \lambda_1 \epsilon_{12} R_2 - (\gamma_1 + \mu)J_1 \quad (\text{S21})$$

$$\frac{dJ_2}{dt} = \lambda_2 \epsilon_{21} R_1 - (\gamma_2 + \mu)J_2 \quad (\text{S22})$$

$$\frac{dR}{dt} = \gamma_1 J_1 + \gamma_2 J_2 - \rho_1 R - \rho_2 R - \mu R \quad (\text{S23})$$

where S represents the proportion of individuals who are fully susceptible to infections by both strains; I_1 represents the proportion of individuals who are infected with strain 1 without prior immunity; I_2 represents the proportion of individuals who are infected with strain 2 without prior immunity; R_1 represents the proportion of individuals who are fully immune against strain 1 and partially susceptible to reinfection by strain 2; R_2 represents the proportion of individuals who are fully immune against strain 2 and partially susceptible to reinfection by strain 1; J_1 represents the proportion of individuals who are infected with strain 1 with prior immunity against strain 2; J_2 represents the proportion of individuals who are infected with strain 2 with prior immunity against strain 1; R represents the proportion of individuals who are immune to infections from both strains; μ represents the birth/death rate; λ_1 and λ_2 represent the force of infection from strains 1 and 2, respectively; ρ_1 and ρ_2 represent the waning immunity rate; γ_1 and γ_2 represent the recovery rate; ϵ_{12} and ϵ_{21} represent the susceptibility to reinfection with strains 2 and 1, respectively, given prior immunity from infection with strains 1 and 2, respectively. The force of infection is modeled as follows:

$$\beta_1 = b_1(1 + \theta_1 \sin(2\pi(t - \phi_1)))\alpha(t) \quad (\text{S24})$$

$$\beta_2 = b_2(1 + \theta_2 \sin(2\pi(t - \phi_2)))\alpha(t) \quad (\text{S25})$$

$$\lambda_1 = \beta_1(I_1 + J_1) \quad (\text{S26})$$

$$\lambda_2 = \beta_2(I_2 + J_2) \quad (\text{S27})$$

In Supplementary Figures S2–S4, we assumed the following parameters: $b_1 = 2 \times 52/\text{years}$, $b_2 = 4 \times 52/\text{years}$, $\phi_1 = \phi_2 = 0$, $\epsilon_{12} = 0.9$, $\epsilon_{21} = 0.5$, $\gamma_1 = \gamma_2 = 52/\text{years}$, $\rho_1 = \rho_2 = 1/\text{years}$, and $\mu = 1/70/\text{years}$. For all simulations, we assumed a 50% transmission reduction for 6 months from 2020:

$$\alpha(t) = \begin{cases} 0.5 & 2020 \leq t < 2020.5 \\ 1 & \text{otherwise} \end{cases} \quad (\text{S28})$$

The seasonal amplitude θ is varied from 0 to 0.4. All simulations were ran from 1900 to 2030 with following initial conditions: $S(0) = 1 - 2 \times 10^{-6}$, $I_1(0) = 1 \times 10^{-6}$, $I_2(0) = 1 \times 10^{-6}$, $R_1(0) = 0$, $R_2(0) = 0$, $J_1(0) = 0$, $J_2(0) = 0$, and $R(0) = 0$.

We considered three scenarios for measuring pathogen resilience: (1) we only have information about strain 1, (2) we only have information about strain 2, and (3) we are unable to distinguish between strains. In the first two scenarios (see panels A–C for strain 1 and panels D–F for strain 2), we considered the dynamics of average susceptibility for each strain and total prevalence:

$$\bar{S}_1 = S + \epsilon_{12}R_2 \quad (\text{S29})$$

$$\hat{I}_1 = I_1 + J_1 \quad (\text{S30})$$

$$\bar{S}_2 = S + \epsilon_{21}R_1 \quad (\text{S31})$$

$$\hat{I}_2 = I_2 + J_2 \quad (\text{S32})$$

630 In the third scenario (panels G–I), we considered the dynamics of total susceptible
631 and infected populations:

$$\hat{S} = S + R_2 + R_1 \quad (\text{S33})$$

$$\hat{I} = I_1 + J_1 + I_2 + J_2 \quad (\text{S34})$$

632 These quantities were used to compute the normalized distance from the attractor,
633 as described in the main text.

634 Estimating intrinsic resilience using mechanistic model

635 We tested whether we can reliably estimate the intrinsic resilience of a system by fit-
636 ting a mechanistic model. Specifically, we simulated case time series from stochastic
637 SIRS and two-strain models and fitted a simple, deterministic SIRS model using a
638 Bayesian framework.

639 We simulated the models in discrete time with a daily time step ($\Delta t = 1$),
640 incorporating demographic stochasticity:

$$\beta(t) = \mathcal{R}_0 \left(1 + \theta \cos \left(\frac{2\pi t}{364} \right) \right) \alpha(t)(1 - \exp(-\gamma)) \quad (\text{S35})$$

$$\text{FOI}(t) = \beta(t)I(t - \Delta t)/N \quad (\text{S36})$$

$$B(t) \sim \text{Poisson}(\mu N) \quad (\text{S37})$$

$$\Delta S(t) \sim \text{Binom}(S(t - \Delta t), 1 - \exp(-(\text{FOI}(t) + \mu)\Delta t)) \quad (\text{S38})$$

$$N_{SI}(t) \sim \text{Binom}\left(\Delta S(t), \frac{\text{FOI}(t)}{\text{FOI}(t) + \mu}\right) \quad (\text{S39})$$

$$\Delta I(t) \sim \text{Binom}(I(t - \Delta t), 1 - \exp(-(\gamma + \mu)\Delta t)) \quad (\text{S40})$$

$$N_{IR}(t) \sim \text{Binom}\left(\Delta I(t), \frac{\gamma}{\gamma + \mu}\right) \quad (\text{S41})$$

$$\Delta R(t) \sim \text{Binom}(R(t - \Delta t), 1 - \exp(-(\delta + \mu)\Delta t)) \quad (\text{S42})$$

$$N_{RS}(t) \sim \text{Binom}\left(\Delta R(t), \frac{\delta}{\delta + \mu}\right) \quad (\text{S43})$$

$$S(t) = S(t - \Delta t) + N_{RS}(t) + B(t) - \Delta S(t) \quad (\text{S44})$$

$$I(t) = I(t - \Delta t) + N_{SI}(t) - \Delta I(t) \quad (\text{S45})$$

$$R(t) = R(t - \Delta t) + N_{IR}(t) - \Delta R(t) \quad (\text{S46})$$

641 where FOI represent the force of infection; N_{ij} represent the number of individuals
642 moving from compartment i to j on a given day; and $B(t)$ represents the number
643 of new births. We simulated the model on a daily scale—assuming 364 days in a
644 year so that it can be evenly grouped into 52 weeks—with the following parameters:
645 $\mathcal{R}_0 = 3$, $\theta = 0.1$, $\gamma = 1/7/\text{days}$, $\delta = 1/(364 \times 2)/\text{days}$, $\mu = 1/(364 \times 50)/\text{days}$, and
646 $N = 1 \times 10^8$. The model was simulated from 1900 to 2030 assuming $S(0) = N/3$,

⁶⁴⁷ $I(0) = 100$, and $R(0) = N - S(0) - I(0)$. The observed incidence from the model
⁶⁴⁸ was then simulated as follows:

$$C(t) = \text{Beta-Binom}(N_{SI}(t), \rho, k), \quad (\text{S47})$$

⁶⁴⁹ where ρ represents the reporting probability and k represents the overdispersion
⁶⁵⁰ parameter of beta-binomial distribution. Here, we used the beta-binomial distribution
⁶⁵¹ to account for overdispersion in reporting. We assumed $\rho = 0.002$ (i.e., 0.2%
⁶⁵² probability) and $k = 1000$.

⁶⁵³ We used an analogous approach for the two-strain model:

$$\beta_1(t) = b_1 \left(1 + \theta_1 \cos \left(\frac{2\pi(t - \phi_1)}{364} \right) \right) \alpha(t) \quad (\text{S48})$$

$$\beta_2(t) = b_2 \left(1 + \theta_2 \cos \left(\frac{2\pi(t - \phi_2)}{364} \right) \right) \alpha(t) \quad (\text{S49})$$

$$\text{FOI}_1(t) = \beta_1(t)(I_1(t - \Delta t) + J_1(t - \Delta t))/N \quad (\text{S50})$$

$$\text{FOI}_2(t) = \beta_2(t)(I_2(t - \Delta t) + J_2(t - \Delta t))/N \quad (\text{S51})$$

$$B(t) \sim \text{Poisson}(\mu N) \quad (\text{S52})$$

$$\Delta S(t) \sim \text{Binom}(S(t - \Delta t), 1 - \exp(-(\text{FOI}_1(t) + \text{FOI}_2(t) + \mu)\Delta t)) \quad (\text{S53})$$

$$N_{SI_1}(t) \sim \text{Binom}\left(\Delta S(t), \frac{\text{FOI}_1(t)}{\text{FOI}_1(t) + \text{FOI}_2(t) + \mu}\right) \quad (\text{S54})$$

$$N_{SI_2}(t) \sim \text{Binom}\left(\Delta S(t), \frac{\text{FOI}_2(t)}{\text{FOI}_1(t) + \text{FOI}_2(t) + \mu}\right) \quad (\text{S55})$$

$$\Delta I_1(t) \sim \text{Binom}(I_1(t - \Delta t), 1 - \exp(-(\gamma_1 + \mu)\Delta t)) \quad (\text{S56})$$

$$N_{I_1 R_1}(t) \sim \text{Binom}\left(\Delta I_1(t), \frac{\gamma_1}{\gamma_1 + \mu}\right) \quad (\text{S57})$$

$$\Delta I_2(t) \sim \text{Binom}(I_2(t - \Delta t), 1 - \exp(-(\gamma_2 + \mu)\Delta t)) \quad (\text{S58})$$

$$N_{I_2 R_2}(t) \sim \text{Binom}\left(\Delta I_2(t), \frac{\gamma_2}{\gamma_2 + \mu}\right) \quad (\text{S59})$$

$$\Delta R_1(t) \sim \text{Binom}(R_1(t - \Delta t), 1 - \exp(-(\epsilon_{21}\text{FOI}_2(t) + \rho_1 + \mu)\Delta t)) \quad (\text{S60})$$

$$N_{R_1 S}(t) \sim \text{Binom}\left(\Delta R_1(t), \frac{\rho_1}{\epsilon_{21}\text{FOI}_2(t) + \rho_1 + \mu}\right) \quad (\text{S61})$$

$$N_{R_1 J_2}(t) \sim \text{Binom}\left(\Delta R_1(t), \frac{\epsilon_{21}\text{FOI}_2(t)}{\epsilon_{21}\text{FOI}_2(t) + \rho_1 + \mu}\right) \quad (\text{S62})$$

$$\Delta R_2(t) \sim \text{Binom}(R_2(t - \Delta t), 1 - \exp(-(\epsilon_{12}\text{FOI}_1(t) + \rho_2 + \mu)\Delta t)) \quad (\text{S63})$$

$$N_{R_2 S}(t) \sim \text{Binom}\left(\Delta R_2(t), \frac{\rho_2}{\epsilon_{12}\text{FOI}_1(t) + \rho_2 + \mu}\right) \quad (\text{S64})$$

$$N_{R_2 J_1}(t) \sim \text{Binom}\left(\Delta R_2(t), \frac{\epsilon_{12}\text{FOI}_1(t)}{\epsilon_{12}\text{FOI}_1(t) + \rho_2 + \mu}\right) \quad (\text{S65})$$

$$\Delta J_1(t) \sim \text{Binom}(J_1(t - \Delta t), 1 - \exp(-(\gamma_1 + \mu)\Delta t)) \quad (\text{S66})$$

$$N_{J_1R}(t) \sim \text{Binom}\left(\Delta J_1(t), \frac{\gamma_1}{\gamma_1 + \mu}\right) \quad (\text{S67})$$

$$\Delta J_2(t) \sim \text{Binom}(J_2(t - \Delta t), 1 - \exp(-(\gamma_2 + \mu)\Delta t)) \quad (\text{S68})$$

$$N_{J_2R}(t) \sim \text{Binom}\left(\Delta J_2(t), \frac{\gamma_2}{\gamma_2 + \mu}\right) \quad (\text{S69})$$

$$\Delta R(t) \sim \text{Binom}(R(t - \Delta t), 1 - \exp(-(\rho_1 + \rho_2 + \mu)\Delta t)) \quad (\text{S70})$$

$$N_{RR_1}(t) \sim \text{Binom}\left(\Delta R(t), \frac{\rho_1}{\rho_1 + \rho_2 + \mu}\right) \quad (\text{S71})$$

$$N_{RR_2}(t) \sim \text{Binom}\left(\Delta R(t), \frac{\rho_2}{\rho_1 + \rho_2 + \mu}\right) \quad (\text{S72})$$

$$S(t) = S(t - \Delta t) - \Delta S(t) + B(t) + N_{R_1S}(t) + N_{R_2S}(t) \quad (\text{S73})$$

$$I_1(t) = I_1(t - \Delta t) - \Delta I_1(t) + N_{SI_1}(t) \quad (\text{S74})$$

$$I_2(t) = I_2(t - \Delta t) - \Delta I_2(t) + N_{SI_2}(t) \quad (\text{S75})$$

$$R_1(t) = R_1(t - \Delta t) - \Delta R_1(t) + N_{I_1R_1}(t) + N_{RR_1}(t) \quad (\text{S76})$$

$$R_2(t) = R_2(t - \Delta t) - \Delta R_2(t) + N_{I_2R_2}(t) + N_{RR_2}(t) \quad (\text{S77})$$

$$J_1(t) = J_1(t - \Delta t) - \Delta J_1(t) + N_{R_2J_1}(t) \quad (\text{S78})$$

$$J_2(t) = J_2(t - \Delta t) - \Delta J_2(t) + N_{R_1J_2}(t) \quad (\text{S79})$$

$$R(t) = R(t - \Delta t) - \Delta R(t) + N_{J_1R}(t) + N_{J_2R}(t) \quad (\text{S80})$$

We simulated the model on a daily scale with previously estimated parameters for the RSV-HMPV interaction [24]: $b_1 = 1.7/\text{weeks}$, $b_2 = 1.95/\text{weeks}$, $\theta_1 = 0.4$, $\theta_2 = 0.3$, $\phi_1 = 0.005 \times 7/364$, $\phi_2 = 4.99 \times 7/364$, $\epsilon_{12} = 0.92$, $\epsilon_{21} = 0.45$, $\gamma_1 = 1/10/\text{days}$, $\gamma_2 = 1/10/\text{days}$, $\rho_1 = 1/364/\text{days}$, $\rho_2 = 1/364/\text{days}$, $\mu = 1/(70 \times 364)/\text{days}$, and $N = 1 \times 10^8$. The model was simulated from 1900 to 2030 assuming $S(0) = N - 200$, $I_1(0) = 100$, $I_2(0) = 100$, $R_1(0) = 0$, $R_2(0) = 0$, $J_1(0) = 0$, $J_2(0) = 0$, and $R(0) = 0$. The observed incidence for each strain is then simulated as follows:

$$C_1(t) = \text{Beta-Binom}(N_{SI_1}(t) + N_{R_2J_1}, \rho, k), \quad (\text{S81})$$

$$C_2(t) = \text{Beta-Binom}(N_{SI_2}(t) + N_{R_1J_2}, \rho, k), \quad (\text{S82})$$

where ρ represents the reporting probability and k represents the overdispersion parameter of beta-binomial distribution. We assumed $\rho = 0.002$ (i.e., 0.2% probability) and $k = 500$. We also considered the total incidence: $C_{\text{total}}(t) = C_1(t) + C_2(t)$.

For both models, we considered a more realistically shaped pandemic perturbation $\alpha(t)$ to challenge our ability to estimate the intervention effects. Thus, we assumed a 40% transmission reduction for 3 months from March 2020, followed by a 10% transmission reduction for 6 months, 20% transmission reduction for 3 months,

668 and a final return to normal levels:

$$\alpha(t) = \begin{cases} 1 & t < 2020.25 \\ 0.6 & 2020.25 \leq t < 2020.5 \\ 0.9 & 2020.5 \leq t < 2021 \\ 0.8 & 2021 \leq t < 2021.25 \\ 1 & 2021.25 \leq t \end{cases}. \quad (\text{S83})$$

669 For all simulations, we truncated the time series from the beginning of 2014 to the
670 end of 2023 and aggregate them into weekly cases.

671 To infer intrinsic resilience from time series, we fitted a simple discrete time,
672 deterministic SIRS model [4]:

$$\Delta t = 1 \text{ week} \quad (\text{S84})$$

$$\text{FOI}(t) = \beta(t)(I(t - \Delta t) + \omega)/N \quad (\text{S85})$$

$$\Delta S(t) = [1 - \exp(-(\text{FOI}(t) + \mu)\Delta t)] S(t - \Delta t) \quad (\text{S86})$$

$$N_{SI}(t) = \frac{\text{FOI}(t)\Delta S(t)}{\text{FOI}(t) + \mu} \quad (\text{S87})$$

$$\Delta I(t) = [1 - \exp(-(\gamma + \mu)\Delta t)] I(t - \Delta t) \quad (\text{S88})$$

$$N_{IR}(t) = \frac{\gamma \Delta I(t)}{\gamma + \mu} \quad (\text{S89})$$

$$\Delta R(t) = [1 - \exp(-(\nu + \mu)\Delta t)] R(t - \Delta t) \quad (\text{S90})$$

$$N_{RS}(t) = \frac{\nu \Delta R(t)}{\nu + \mu} \quad (\text{S91})$$

$$S(t) = S(t - \Delta t) + \mu S - \Delta S(t) + N_{RS}(t) \quad (\text{S92})$$

$$I(t) = I(t - \Delta t) - \Delta I(t) + N_{SI}(t) \quad (\text{S93})$$

$$R(t) = R(t - \Delta t) - \Delta R(t) + N_{IR}(t) \quad (\text{S94})$$

673 where we include an extra term ω to account for external infections. Although actual
674 simulations did not include any external infections, we found that including this term
675 generally helped with model convergence in previous analyses [4]. The transmission
676 rate was divided into a seasonal term $\beta_{\text{seas}}(t)$ (repeated every year) and intervention
677 term $\alpha(t)$, which were estimated jointly:

$$\beta(t) = \beta_{\text{seas}}(t)\alpha(t), \quad (\text{S95})$$

678 where $\alpha < 1$ corresponds to reduction in transmission due to intervention effects. To
679 constrain the smoothness of $\beta_{\text{seas}}(t)$, we imposed cyclic, random-walk priors:

$$\beta_{\text{seas}}(t) \sim \text{Normal}(\beta_{\text{seas}}(t - 1), \sigma) \quad t = 2 \dots 52 \quad (\text{S96})$$

$$\beta_{\text{seas}}(1) \sim \text{Normal}(\beta_{\text{seas}}(52), \sigma) \quad (\text{S97})$$

680 [SWP: I noticed that I forgot to put a prior on σ so need to re-do this but won't
 681 change the results.] We fixed $\alpha(t) = 1$ for all $t < 2020$ and estimate α assuming a
 682 normal prior:

$$\alpha \sim \text{Normal}(1, 0.25). \quad (\text{S98})$$

683 We assumed weakly informative priors on ω and ν :

$$\omega \sim \text{Normal}(0, 200) \quad (\text{S99})$$

$$\nu \sim \text{Normal}(104, 26) \quad (\text{S100})$$

684 We assumed that the true birth/death rates, population sizes, and recovery rates are
 685 known. We note, however, that assuming $\gamma = 1/\text{week}$ actually corresponds to a mean
 686 simulated infectious period of 1.6 weeks, which is much longer than the true value;
 687 this approximation allows us to test whether we can still robustly estimate the in-
 688 trinsic resilience given parameter mis-specification. Initial conditions were estimated
 689 with following priors:

$$S(0) = Ns(0) \quad (\text{S101})$$

$$I(0) = Ni(0) \quad (\text{S102})$$

$$s(0) \sim \text{Uniform}(0, 1) \quad (\text{S103})$$

$$i(0) \sim \text{Half-Normal}(0, 0.001) \quad (\text{S104})$$

690 Finally, the observation model was specified as follows:

$$\text{Cases}(t) \sim \text{Negative-Binomial}(\rho N_{SI}(t), \phi) \quad (\text{S105})$$

$$\rho \sim \text{Half-Normal}(0, 0.02) \quad (\text{S106})$$

$$\phi \sim \text{Half-Normal}(0, 10) \quad (\text{S107})$$

691 where ρ represents the reporting probability and ϕ represents the negative binomial
 692 overdispersion parameter.

693 The model was fitted to four separate time series: (1) incidence time series from
 694 the SIRS model, (2) incidence time series for strain 1 from the two-strain model,
 695 (3) incidence time series for strain 2 from the two-strain model, and (4) combined
 696 incidence time series for strains 1 and 2 from the two-strain model. The model was
 697 fitted using rstan [34, 35]. The resulting posterior distribution was used to calculate
 698 the intrinsic resilience of the seasonally unforced system with the same parameters;
 699 eigenvalues of the discrete-time SIR model were computed by numerically finding
 700 the equilibrium and calculating the Jacobian matrix.

701 Validations for window-selection criteria

702 We used stochastic SIRS simulations to identify optimal parameters for the window-
 703 selection criteria that we used for the linear regression for estimating empirical re-
 704 silience. For each simulation, we began by generating a random perturbation $\alpha(t)$

705 from a random set of parameters. First, we drew the duration of intervention τ_{npi}
 706 from a uniform distribution between 1 and 2 years. Then, we drew independent
 707 normal variables z_i of length $\lfloor 364\tau_{\text{npi}} \rfloor$ with a standard deviation of 0.02 and took a
 708 reverse cumulative sum to obtain a realistic shape for the intervention:

$$x_n = 1 + \sum_{i=n}^{\lfloor 364\tau_{\text{npi}} \rfloor} z_i, \quad n = 1, \dots, \lfloor 364\tau_{\text{npi}} \rfloor. \quad (\text{S108})$$

709 We repeated this random generation process until less than 10% of x_n exceeds 1—
 710 this was done to prevent the perturbation $\alpha(t)$ stays below 1 (and therefore reduce
 711 transmission) for the most part. Then, we set any values that are above 1 or below 0
 712 as 1 and 0, respectively. Then, we randomly drew the minimum transmission during
 713 intervention α_{\min} from a uniform distribution between 0.5 and 0.7 and scale x_n to
 714 have a minimum of α_{\min} :

$$x_{\text{scale},n} = \alpha_{\min} + (1 - \alpha_{\min}) \times \frac{x_n - \min x_n}{1 - \min x_n}. \quad (\text{S109})$$

715 This allowed us to simulate a realistically shaped intervention:

$$\alpha(t) = \begin{cases} 1 & t < 2020 \\ x_{\text{scale},364(t-2020)} & 2020 \leq t < 2020 + \tau_{\text{npi}} \\ 1 & \tau_{\text{npi}} \leq t \end{cases}. \quad (\text{S110})$$

716 Given this intervention function, we draw \mathcal{R}_0 from a uniform distribution between 1.5
 717 and 4 and the mean duration of immunity $1/\delta$ from a uniform distribution between
 718 1 and 4. Then, we simulate the stochastic SIRS model from $S(0) = 10^8/\mathcal{R}_0$ and
 719 $I(0) = 100$ from 1990 to 2025 and truncate the time series to 2014–2025; if the
 720 epidemic becomes extinct before the end of simulation, we discard that simulation
 721 and start over from the intervention generation step.

722 For each epidemic simulation, we computed the empirical resilience by varying
 723 the threshold R for the nearest neighbor approach from 4 to 14 with increments of
 724 2, the number of divisions K for the window selection between 8 and 25, and the
 725 truncation threshold a for the window selection between 1 to 3; this was done for all
 726 possible combinations of R , K , and a . We also compared this with the naive approach
 727 that uses the entire distance-from-attractor time series, starting from the maximum
 728 distance to the end of the time series. We repeated this procedure 500 times and
 729 quantified the correlation between empirical and intrinsic resilience estimates across
 730 two approaches.

Supplementary Figures

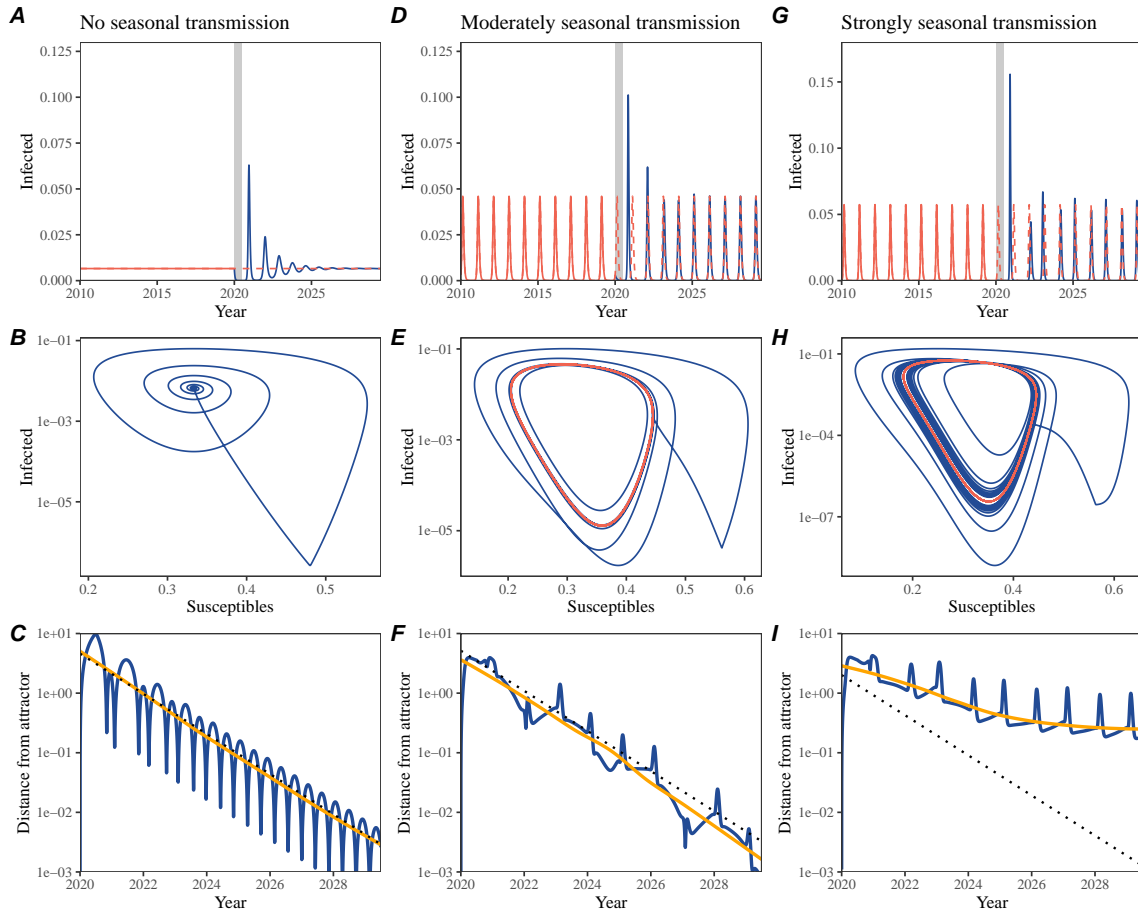


Figure S1: Impact of seasonal transmission on pathogen resilience. (A, D, G) Simulated epidemic trajectories using the SIRS model without seasonal forcing (A), with seasonal forcing of amplitude of 0.2 (D), and with seasonal forcing of amplitude of 0.4 (G). Red and blue solid lines represent epidemic dynamics before and after interventions are introduced, respectively. Red dashed lines represent counterfactual epidemic dynamics in the absence of interventions. Gray regions indicate the duration of interventions. (B, E, H) Phase plane representation of the time series in panels A, D, and G alongside the corresponding susceptible host dynamics. Red and blue solid lines represent epidemic trajectories on an SI phase plane before and after interventions are introduced, respectively. (C, F, I) Changes in logged distance from the attractor over time. Blue lines represent the logged distance from the attractor. Orange lines represent the locally estimated scatterplot smoothing (LOESS) fits to the logged distance from the attractor. Dotted lines show the intrinsic resilience of the seasonally unforced system.

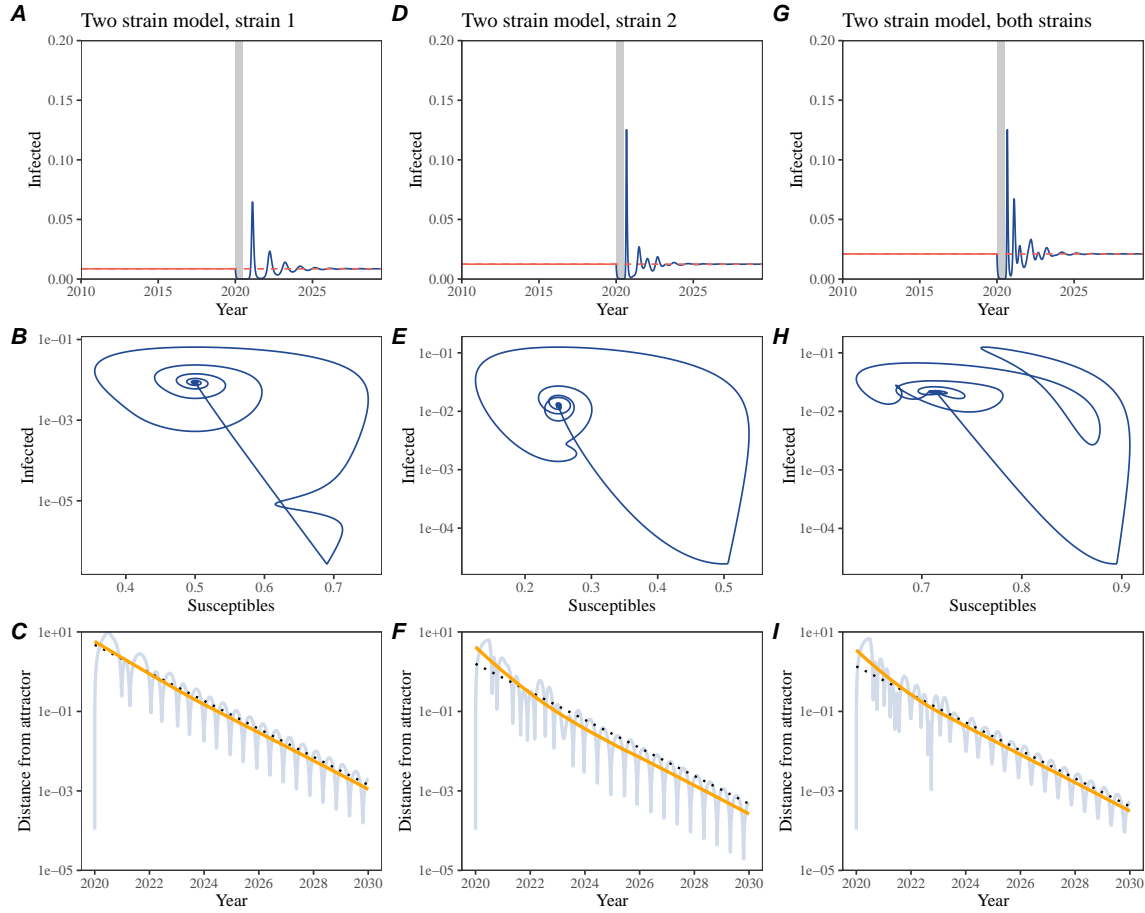


Figure S2: A simple method to measure pathogen resilience following pandemic perturbations for a two-strain system without seasonal forcing. (A, D, G) Simulated epidemic trajectories using a multi-strain system without seasonal forcing. Red and blue solid lines represent epidemic dynamics before and after interventions are introduced, respectively. Red dashed lines represent counterfactual epidemic dynamics in the absence of interventions. Gray regions indicate the duration of interventions. (B, E, H) Phase plane representation of the time series in panels A, D, and G alongside the corresponding susceptible host dynamics. Blue solid lines represent epidemic trajectories on an SI phase plane before and after interventions are introduced, respectively. (C, F, I) Changes in logged distance from the attractor over time. Blue lines represent the logged distance from the attractor. Orange lines represent the locally estimated scatterplot smoothing (LOESS) fits to the logged distance from the attractor. Dotted lines show the intrinsic resilience of the seasonally unforced system.

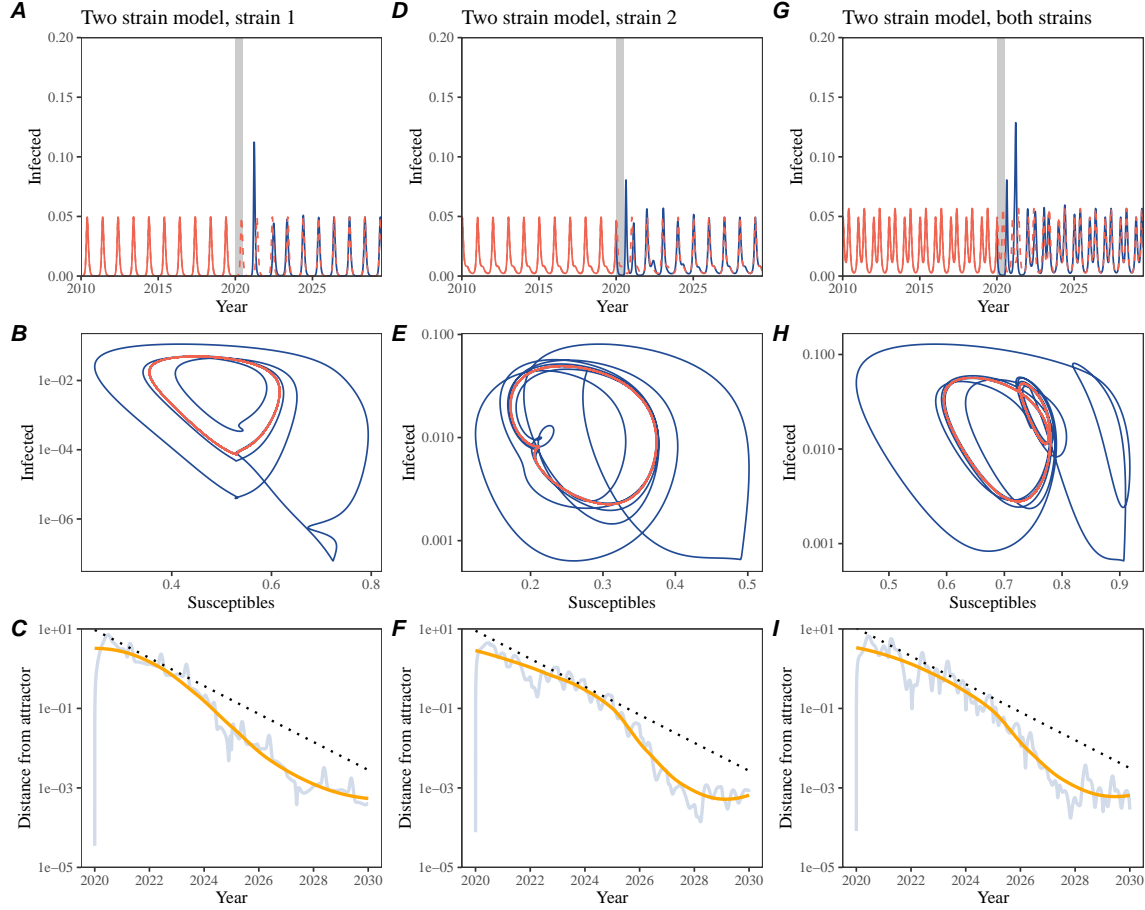


Figure S3: A simple method to measure pathogen resilience following pandemic perturbations for a two-strain system with seasonal forcing. (A, D, G) Simulated epidemic trajectories using a two-strain system with seasonal forcing (amplitude of 0.2). In this model, two strains compete through cross immunity. Red and blue solid lines represent epidemic dynamics before and after interventions are introduced, respectively. Red dashed lines represent counterfactual epidemic dynamics in the absence of interventions. Gray regions indicate the duration of interventions. (B, E, H) Phase plane representation of the time series in panels A, D, and G alongside the corresponding susceptible host dynamics. Red and blue solid lines represent epidemic trajectories on an SI phase plane before and after interventions are introduced, respectively. (C, F, I) Changes in logged distance from the attractor over time. Blue lines represent the logged distance from the attractor. Orange lines represent the locally estimated scatterplot smoothing (LOESS) fits to the logged distance from the attractor. Dotted lines show the intrinsic resilience of the seasonally unforced system.

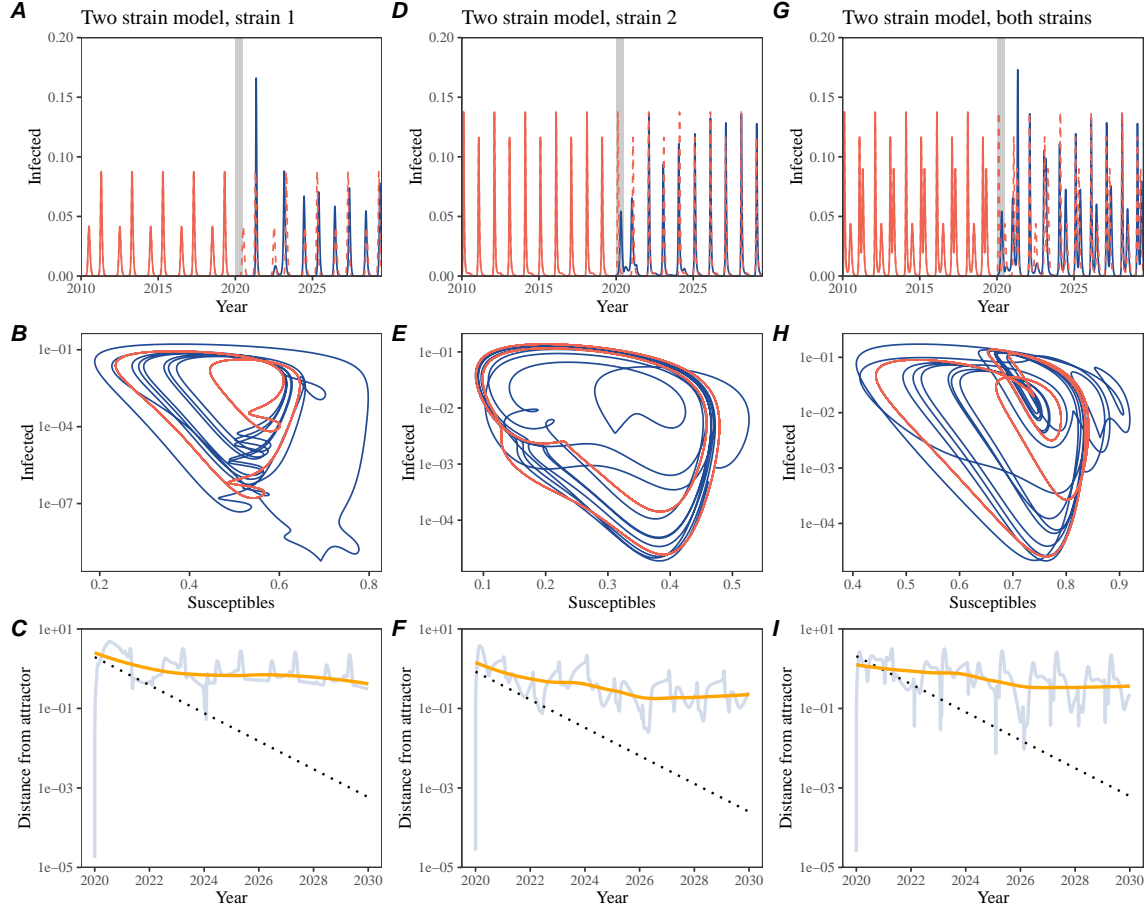


Figure S4: A simple method to measure pathogen resilience following pandemic perturbations for a multi-strain system with strong seasonal forcing. (A, D, G) Simulated epidemic trajectories using a multi-strain system with seasonal forcing (amplitude of 0.4). In this model, two strains compete through cross immunity. Red and blue solid lines represent epidemic dynamics before and after interventions are introduced, respectively. Red dashed lines represent counterfactual epidemic dynamics in the absence of interventions. Gray regions indicate the duration of interventions. (B, E, H) Phase plane representation of the time series in panels A, D, and G alongside the corresponding susceptible host dynamics. Red and blue solid lines represent epidemic trajectories on an SI phase plane before and after interventions are introduced, respectively. (C, F, I) Changes in logged distance from the attractor over time. Blue lines represent the logged distance from the attractor. Orange lines represent the locally estimated scatterplot smoothing (LOESS) fits to the logged distance from the attractor. Dotted lines show the intrinsic resilience of the seasonally unforced system.

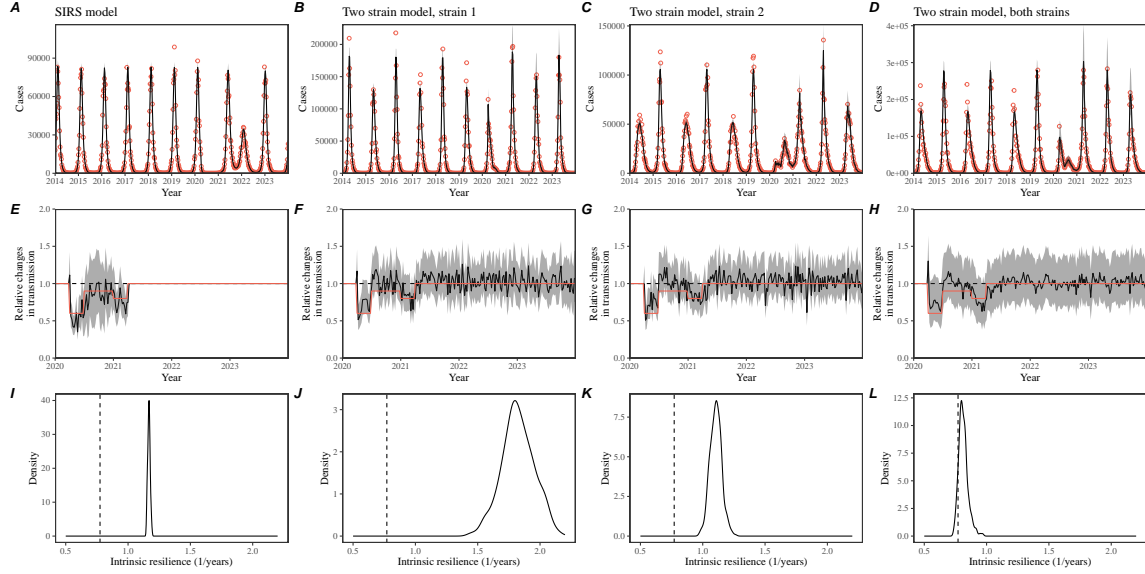


Figure S5: Mechanistic model fits to simulated data and inferred intrinsic resilience. We simulated discrete time, stochastic epidemic trajectories using seasonally forced SIRS model (A,E,I) and seasonally forced two-strain model (B–D, F–H, and J–L) and tested whether we can estimate the intrinsic resilience of the seasonally unforced versions of the model by fitting a mechanistic model (Supplementary Text). We fitted the same discrete time, deterministic SIRS model across all four scenarios. (A–D) Simulated case time series from corresponding models shown in the title (red) and SIRS model fits (black). (E–H) Assumed changes in transmission due to pandemic perturbations (red) and estimated time-varying relative transmission rates for the perturbation impact from the SIRS model fits (black). Solid lines and shaded regions represent fitted posterior median and 95% credible intervals. (I–L) True intrinsic resilience of the seasonally unforced system (vertical lines) and the posterior distribution of the inferred intrinsic resilience from the SIRS model (density plots).

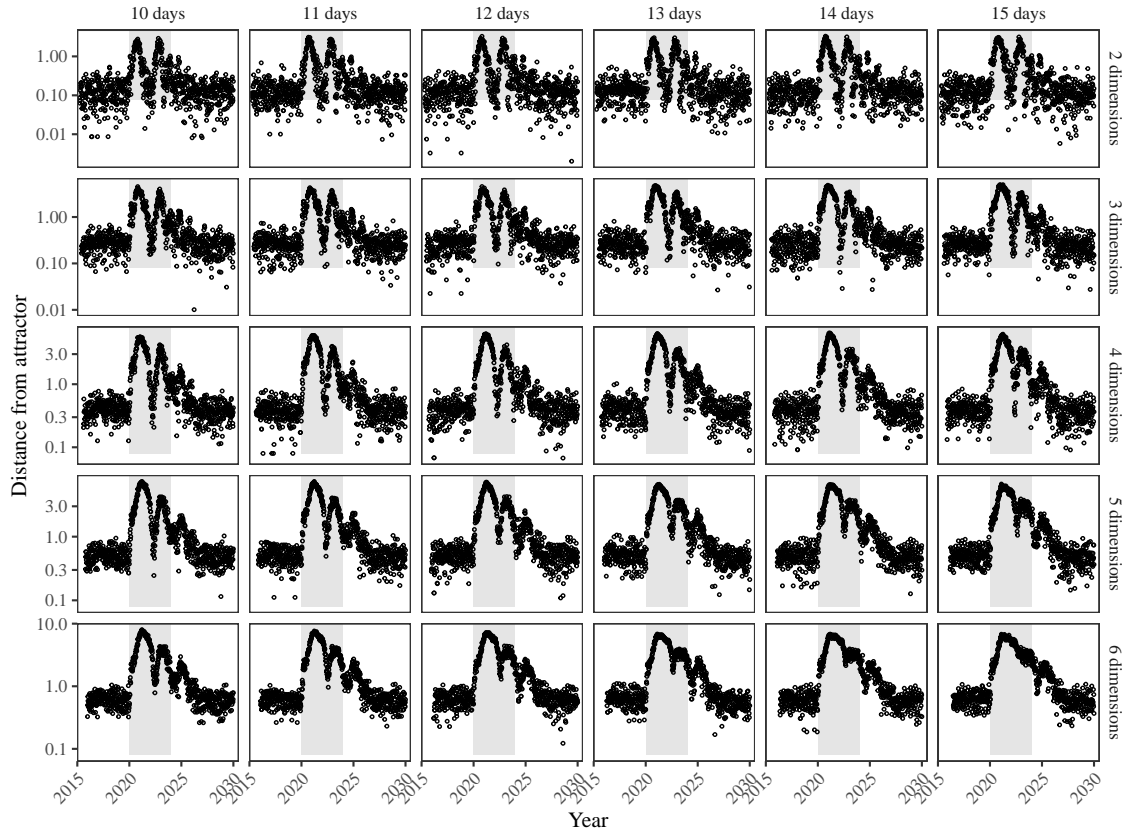


Figure S6: Sensitivity of the distance from the attractor to choices about embedding lags and dimensions. Sensitivity analysis for the distance-from-attractor time series shown in Figure 3E in the main text by varying the embedding lag between 10–15 days and embedding dimensions between 2–6 dimensions. [SWP: You said: “Did you do sensitivity analyses with other systems or just this one? I think we’ll probably need to do it with several systems”. I think it’s OK to just do this because we’re just trying to show qualitatively that longer lags and higher dimensions smooth things out. We also explore resilience of other models in other figures.]

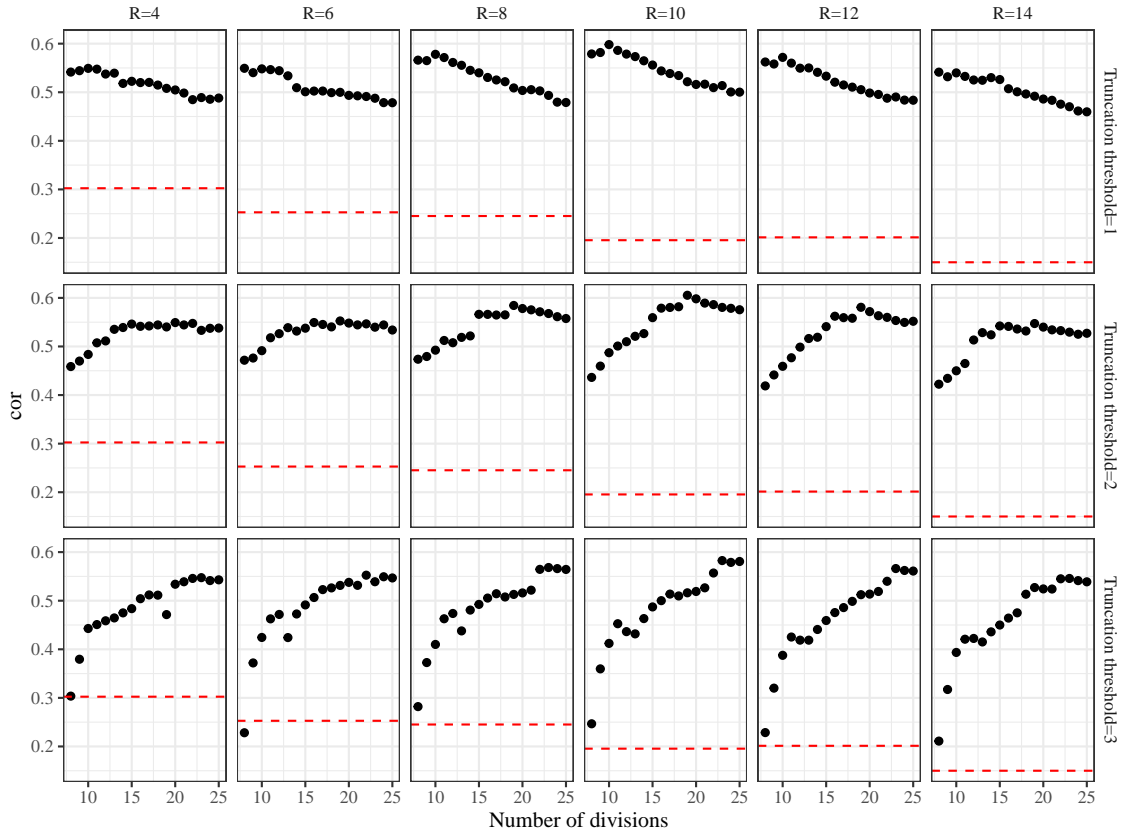


Figure S7: Impact of fitting window selection on the estimation of empirical resilience. We simulated 500 epidemics of a stochastic SIRS model with randomly drawn parameters and randomly generated pandemic perturbations (Supplementary Text). For each simulation, we varied the false nearest neighbor threshold R for reconstructing the empirical attractor as well as the parameters for regression window selection (i.e., the truncation threshold a and the the number of divisions K). Each point represents the resulting correlation coefficient between empirical and intrinsic resilience estimates for a given scenario. Dashed lines represent the correlation coefficient between empirical and intrinsic resilience estimates for the naive approach that fits a linear regression on a log scale, starting from the maximum distance until the end of the time series.

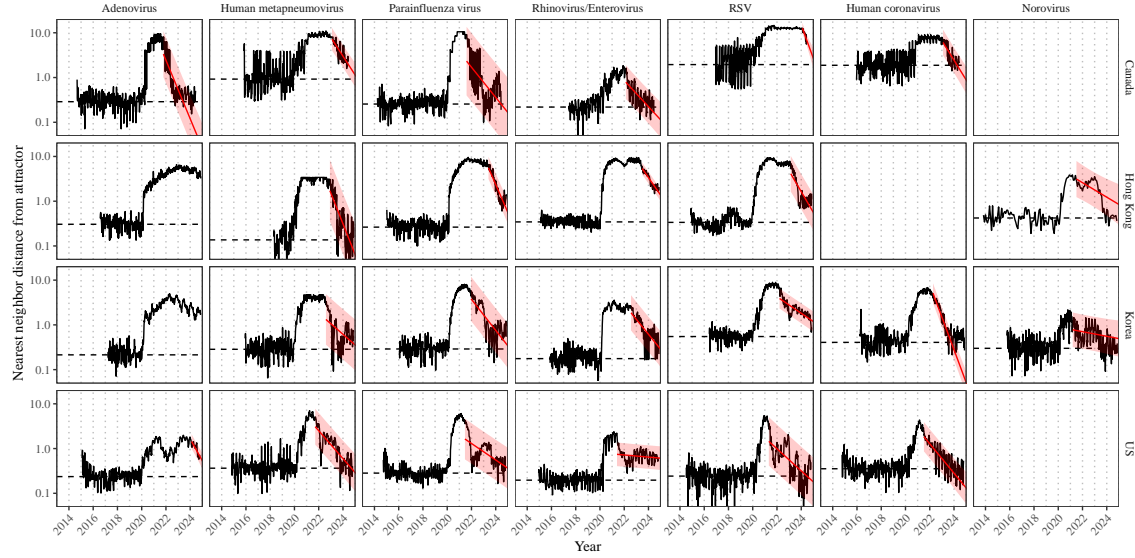


Figure S8: Estimated time series of distance from the attractor for each pathogen and corresponding linear regression fits using automated window selection criterion across Canada, Hong Kong, Korea, and the US. Black lines represent the estimated distance from the attractor. Red lines and shaded regions represent the linear regression fits and corresponding 95% confidence intervals. Dashed lines represent the average of the pre-pandemic nearest neighbor distances.

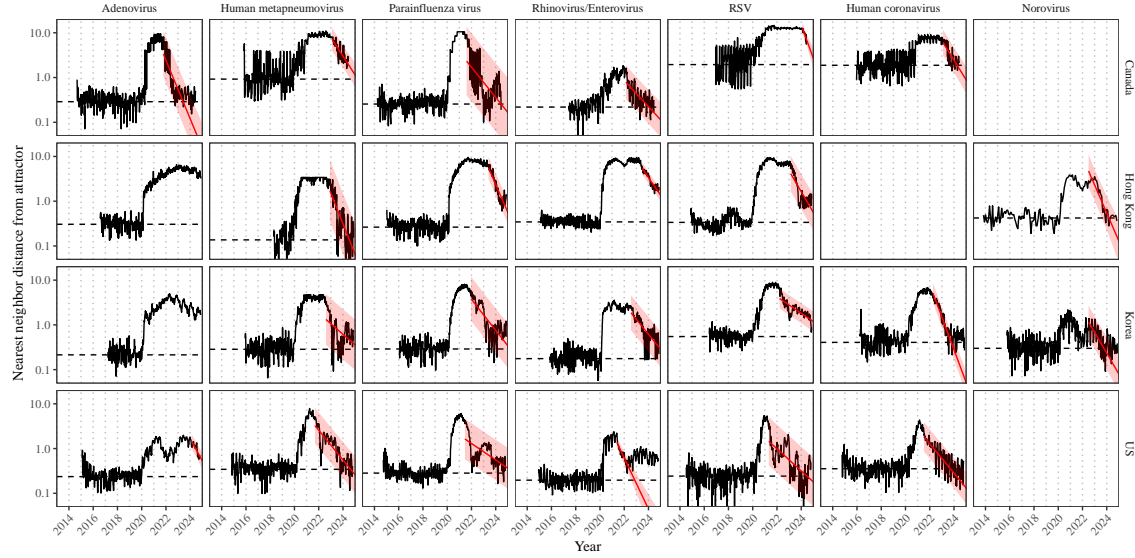


Figure S9: Estimated time series of distance from the attractor for each pathogen and corresponding linear regression fits across Canada, Hong Kong, Korea, and the US, including ad-hoc regression window selection. We used ad-hoc regression windows for norovirus in Hong Kong and Korea and Rhinovirus/Enterovirus in the US. Black lines represent the estimated distance from the attractor. Red lines and shaded regions represent the linear regression fits and corresponding 95% confidence intervals. Dashed lines represent the average of the pre-pandemic nearest neighbor distances.

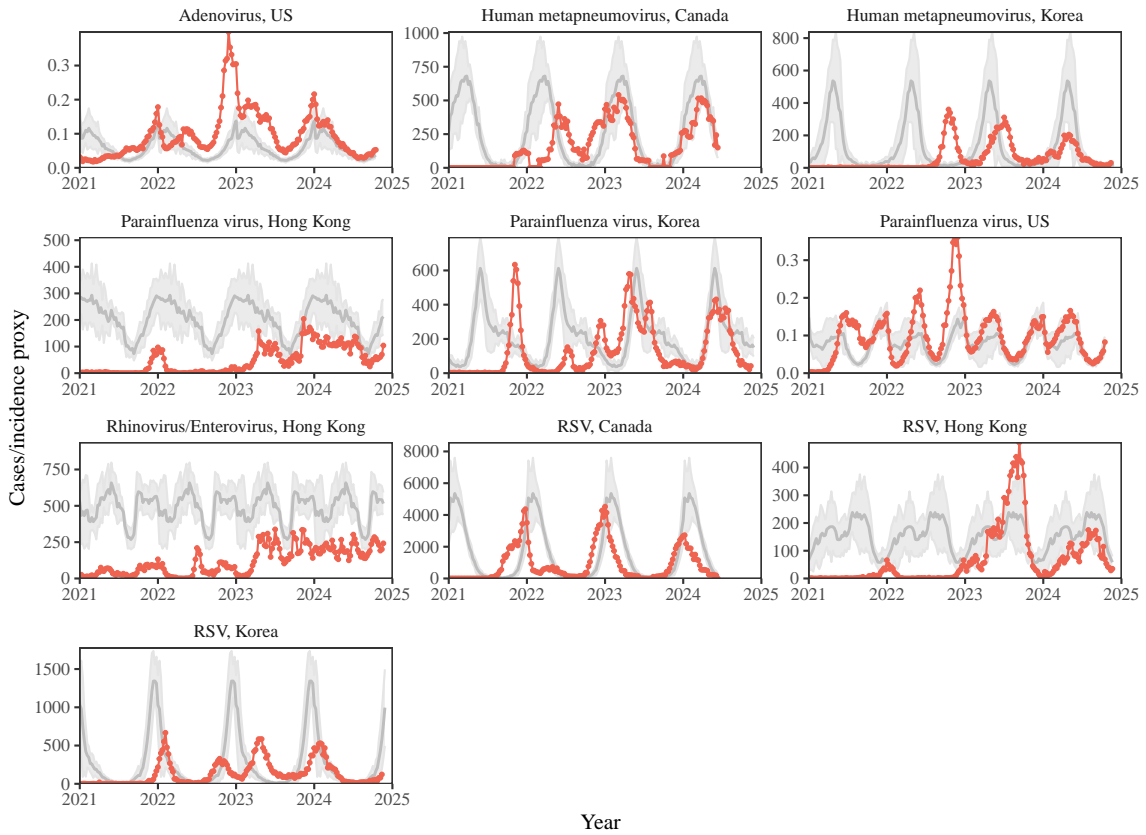


Figure S10: Observed dynamics for pathogen that are predicted to return after the end of 2024. Red points and lines represent data before 2020. Gray lines and shaded regions represent the mean seasonal patterns and corresponding 95% confidence intervals around the mean, previously shown in Figure 1.

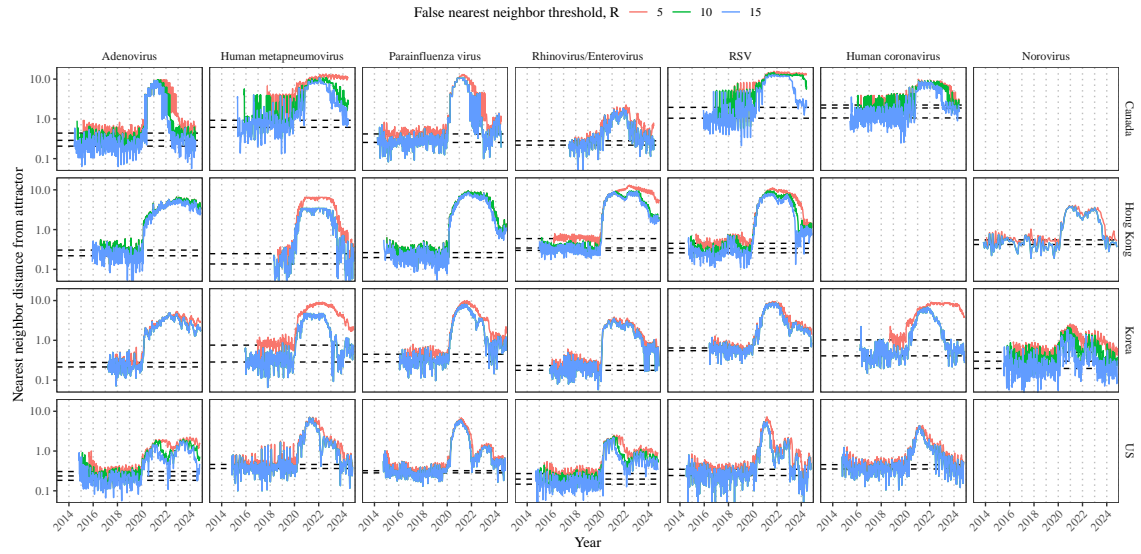


Figure S11: Estimated time series of distance from the attractor for each pathogen across different choices about false nearest neighbor threshold values. Using higher threshold values for the false nearest neighbor approach gives lower embedding dimensions. Colored lines represent the estimated distance from the attractor for different threshold values.

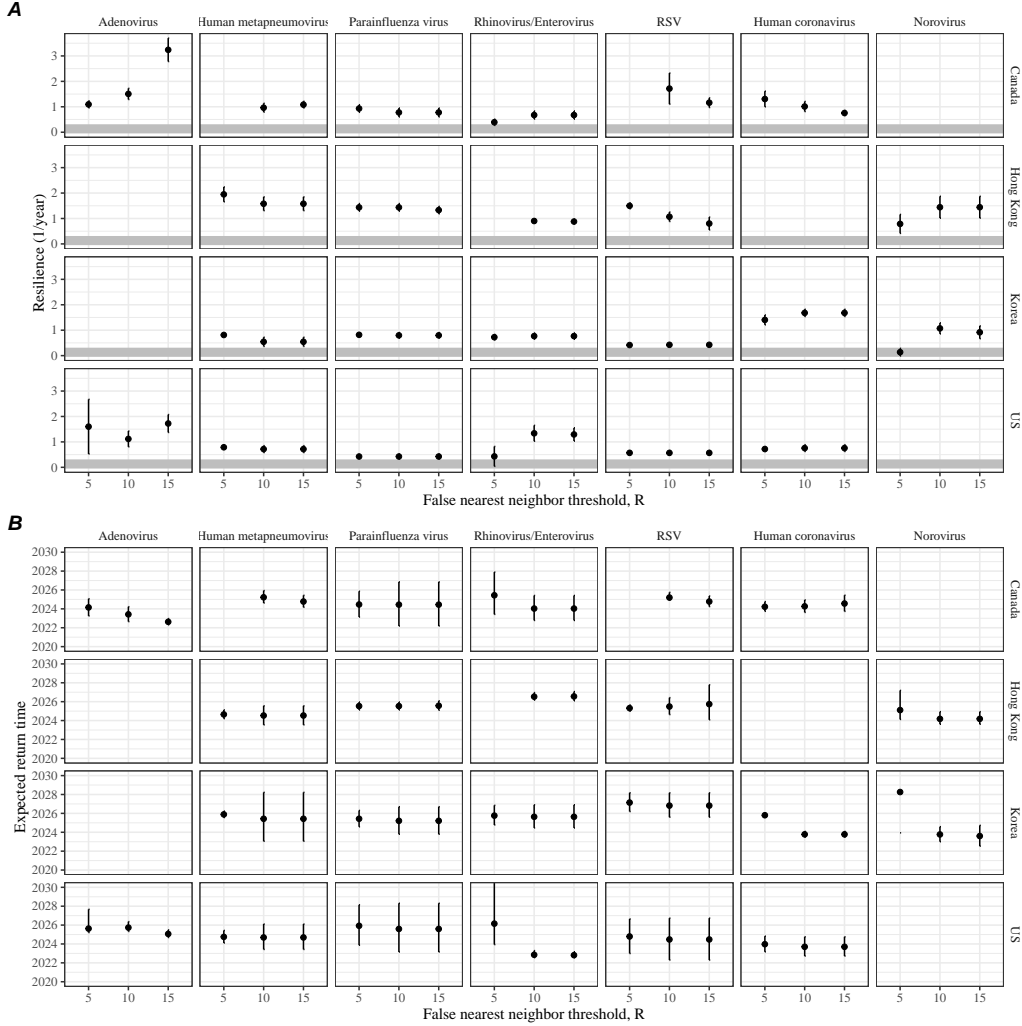


Figure S12: Summary of resilience estimates and predictions for return time across different choices about false nearest neighbor threshold values. The automated window selection method was used for all scenarios to estimate pathogen resilience, except for norovirus in Hong Kong and Korea and Rhinovirus/Enterovirus in the US. We used the same ad-hoc regression windows for norovirus in Hong Kong and Korea and Rhinovirus/Enterovirus in the US as we did in the main analysis. (A) Estimated pathogen resilience. The gray horizontal line represents the intrinsic resilience of pre-vaccination measles dynamics. (B) Predicted timing of when each pathogen will return to their pre-pandemic cycles. The dashed line in panel B indicates the end of 2024 (current observation time). Error bars represent 95% confidence intervals.

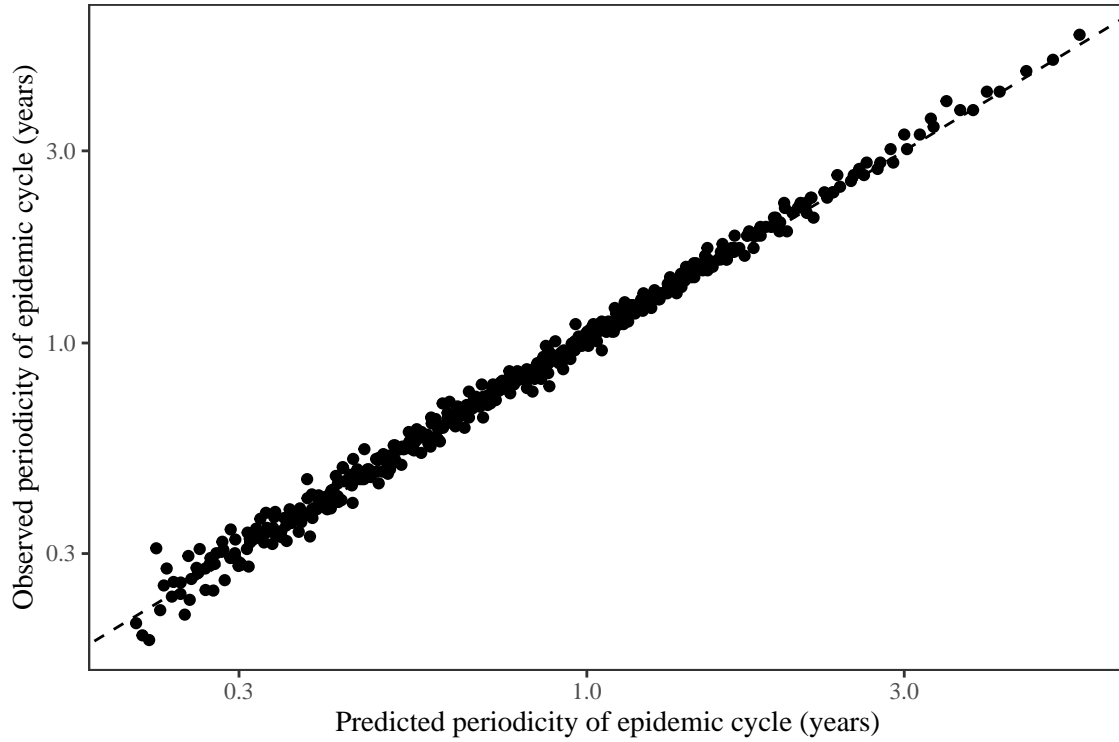


Figure S13: **Comparison between the observed and predicted periodicity of the epidemic cycle of the seasonally unforced SIRS model.** The observed periodicity of the epidemic corresponds to the periodicity at which maximum spectral density occurs. The predicted periodicity of the epidemic corresponds to $2\pi/\text{Im}(\lambda)$, where $\text{Im}(\lambda)$ is the imaginary part of the eigenvalue.

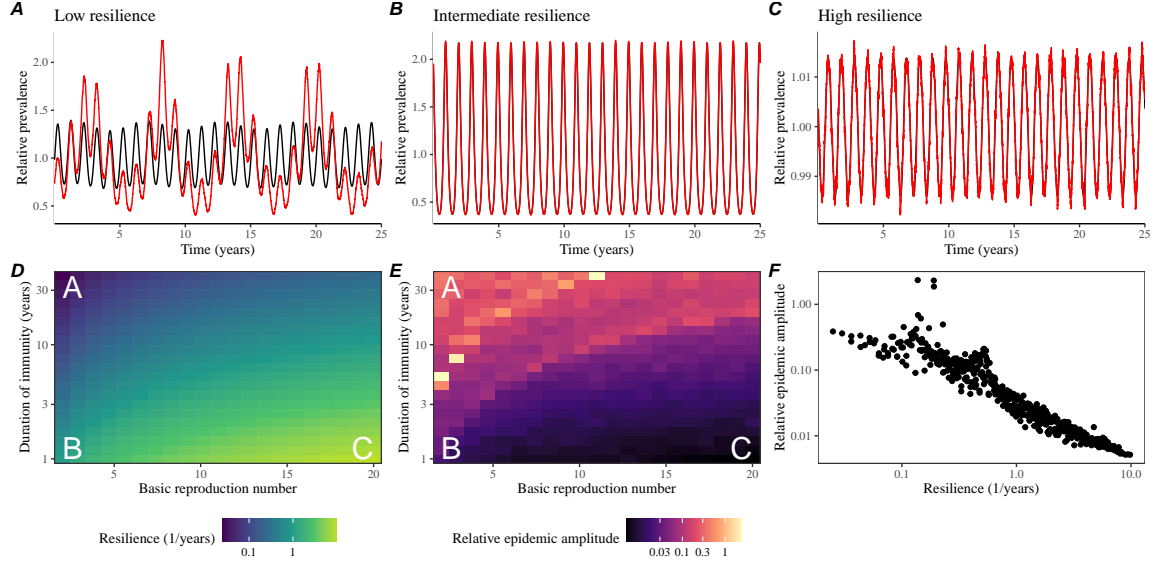


Figure S14: Linking resilience of a host-pathogen system to its sensitivity to stochastic perturbations for the seasonally forced SIRS model. (A–C) Epidemic trajectories of a stochastic SIRS model across three different resilience values: low, intermediate, and high. The relative prevalence was calculated by dividing infection prevalence by its mean value. (D) The heat map represents the intrinsic resilience of the seasonally unforced system as a function of the basic reproduction number \mathcal{R}_0 and the duration of immunity. (E) The heat map represents the relative epidemic amplitude as a function of the basic reproduction number \mathcal{R}_0 and the duration of immunity. To calculate the relative epidemic amplitude, we first take the relative difference in infection prevalence between stochastic and deterministic trajectories: $\epsilon = (I_{\text{stoch}} - I_{\text{det}})/I_{\text{det}}$. Then, we calculate the difference between maximum and minimum of the relative difference and divide by half: $(\max \epsilon - \min \epsilon)/2$. (F) The relationship between pathogen resilience and relative epidemic amplitude.

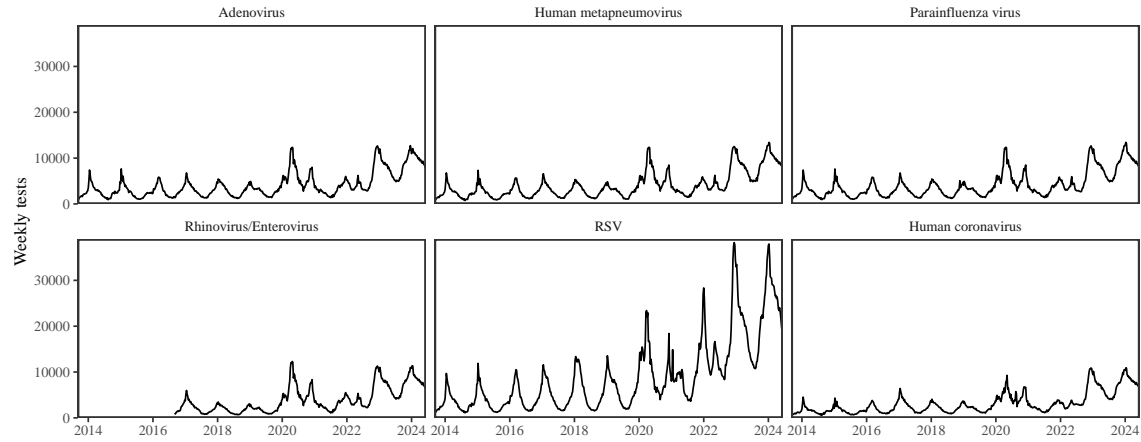


Figure S15: Testing patterns for respiratory pathogens in Canada.

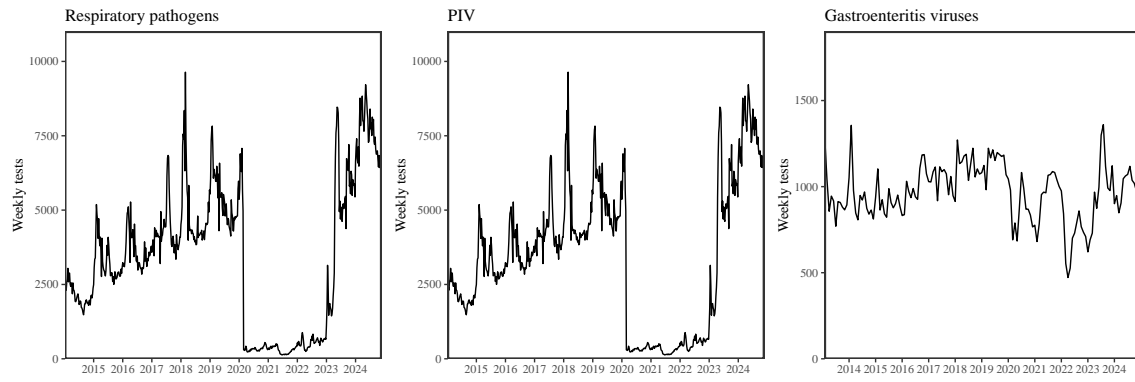


Figure S16: Testing patterns for respiratory pathogens, PIV, and gastroenteritis viruses in Hong Kong.

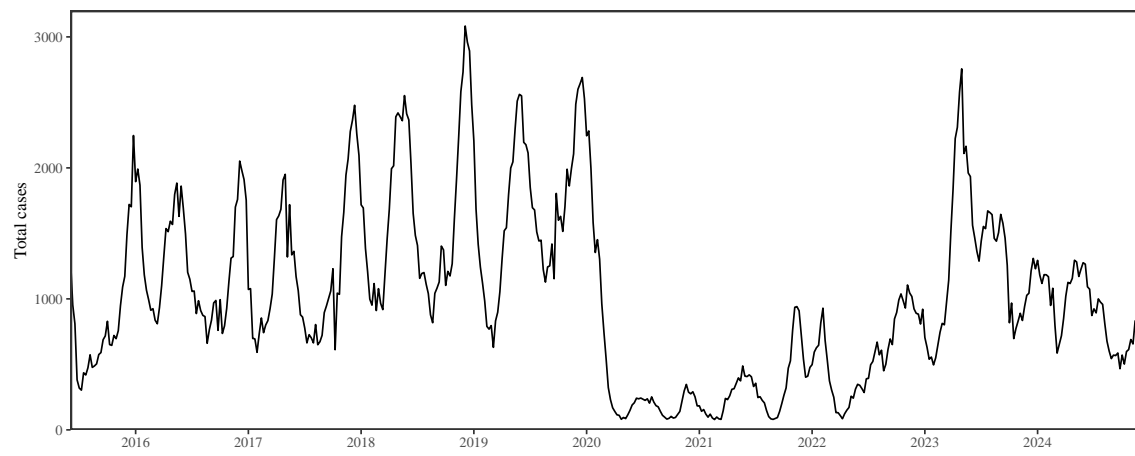


Figure S17: Total number of reported respiratory infection cases in Korea.

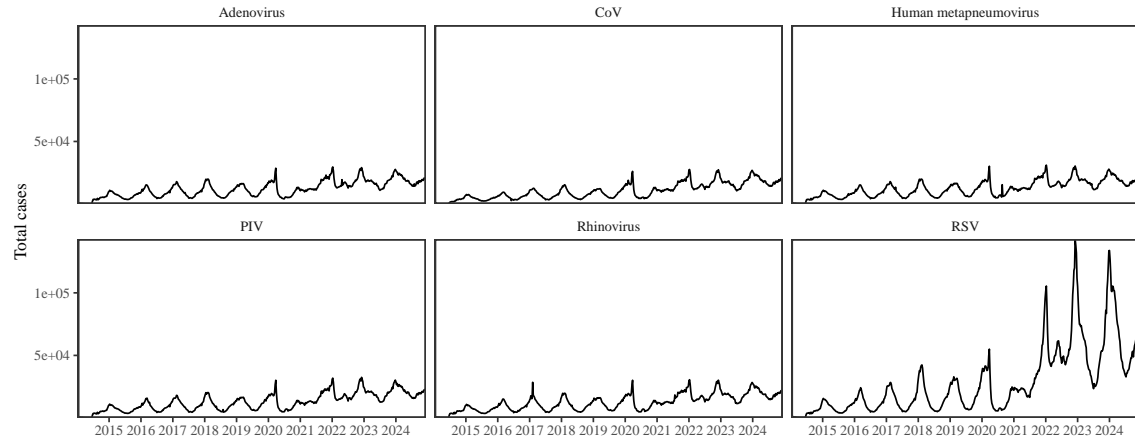


Figure S18: Testing patterns for respiratory pathogens in the US reported through the NREVSS.

732 References

- 733 [1] Rachel E Baker, Sang Woo Park, Wenchang Yang, Gabriel A Vecchi, C Jessica E
734 Metcalf, and Bryan T Grenfell. The impact of COVID-19 nonpharmaceutical
735 interventions on the future dynamics of endemic infections. *Proceedings of the*
736 *National Academy of Sciences*, 117(48):30547–30553, 2020.
- 737 [2] Gabriela B Gomez, Cedric Mahé, and Sandra S Chaves. Uncertain effects of the
738 pandemic on respiratory viruses. *Science*, 372(6546):1043–1044, 2021.
- 739 [3] Mihaly Koltai, Fabienne Krauer, David Hodgson, Edwin van Leeuwen, Marina
740 Treskova-Schwarzbach, Mark Jit, and Stefan Flasche. Determinants of RSV
741 epidemiology following suppression through pandemic contact restrictions. *Epi-*
742 *demics*, 40:100614, 2022.
- 743 [4] Sang Woo Park, Brooklyn Noble, Emily Howerton, Bjarke F Nielsen, Sarah
744 Lentz, Lilliam Ambroggio, Samuel Dominguez, Kevin Messacar, and Bryan T
745 Grenfell. Predicting the impact of non-pharmaceutical interventions against
746 COVID-19 on *Mycoplasma pneumoniae* in the United States. *Epidemics*,
747 49:100808, 2024.
- 748 [5] Amanda C Perofsky, Chelsea L Hansen, Roy Burstein, Shanda Boyle, Robin
749 Prentice, Cooper Marshall, David Reinhart, Ben Capodanno, Melissa Truong,
750 Kristen Schwabe-Fry, et al. Impacts of human mobility on the citywide trans-
751 mission dynamics of 18 respiratory viruses in pre-and post-COVID-19 pandemic
752 years. *Nature communications*, 15(1):4164, 2024.
- 753 [6] Eric J Chow, Timothy M Uyeki, and Helen Y Chu. The effects of the COVID-19
754 pandemic on community respiratory virus activity. *Nature Reviews Microbiol-*
755 *ogy*, 21(3):195–210, 2023.
- 756 [7] Stephen M Kissler, Christine Tedijanto, Edward Goldstein, Yonatan H Grad,
757 and Marc Lipsitch. Projecting the transmission dynamics of SARS-CoV-2
758 through the postpandemic period. *Science*, 368(6493):860–868, 2020.
- 759 [8] Rachel E Baker, Chadi M Saad-Roy, Sang Woo Park, Jeremy Farrar, C Jessica E
760 Metcalf, and Bryan T Grenfell. Long-term benefits of nonpharmaceutical inter-
761 ventions for endemic infections are shaped by respiratory pathogen dynamics.
762 *Proceedings of the National Academy of Sciences*, 119(49):e2208895119, 2022.
- 763 [9] John-Sebastian Eden, Chisha Sikazwe, Ruopeng Xie, Yi-Mo Deng, Sheena G
764 Sullivan, Alice Michie, Avram Levy, Elena Cutmore, Christopher C Blyth,
765 Philip N Britton, et al. Off-season RSV epidemics in Australia after easing
766 of COVID-19 restrictions. *Nature communications*, 13(1):2884, 2022.
- 767 [10] Stuart L Pimm. The structure of food webs. *Theoretical population biology*,
768 16(2):144–158, 1979.

- 769 [11] Michael G Neubert and Hal Caswell. Alternatives to resilience for measuring
770 the responses of ecological systems to perturbations. *Ecology*, 78(3):653–665,
771 1997.
- 772 [12] Lance H Gunderson. Ecological resilience—in theory and application. *Annual
773 review of ecology and systematics*, 31(1):425–439, 2000.
- 774 [13] Vasilis Dakos and Sonia Kéfi. Ecological resilience: what to measure and how.
775 *Environmental Research Letters*, 17(4):043003, 2022.
- 776 [14] Floris Takens. Detecting strange attractors in turbulence. In *Dynamical Sys-
777 tems and Turbulence, Warwick 1980: proceedings of a symposium held at the
778 University of Warwick 1979/80*, pages 366–381. Springer, 2006.
- 779 [15] Jonathan Dushoff, Joshua B Plotkin, Simon A Levin, and David JD Earn.
780 Dynamical resonance can account for seasonality of influenza epidemics. *Pro-
781 ceedings of the National Academy of Sciences*, 101(48):16915–16916, 2004.
- 782 [16] Alan Hastings, Karen C Abbott, Kim Cuddington, Tessa Francis, Gabriel Gell-
783 ner, Ying-Cheng Lai, Andrew Morozov, Sergei Petrovskii, Katherine Scran-
784 ton, and Mary Lou Zeeman. Transient phenomena in ecology. *Science*,
785 361(6406):eaat6412, 2018.
- 786 [17] Matthew B Kennel, Reggie Brown, and Henry DI Abarbanel. Determining
787 embedding dimension for phase-space reconstruction using a geometrical con-
788 struction. *Physical review A*, 45(6):3403, 1992.
- 789 [18] Eugene Tan, Shannon Algar, Débora Corrêa, Michael Small, Thomas Stemler,
790 and David Walker. Selecting embedding delays: An overview of embedding
791 techniques and a new method using persistent homology. *Chaos: An Interdis-
792 ciplinary Journal of Nonlinear Science*, 33(3), 2023.
- 793 [19] Jennifer M Radin, Anthony W Hawksworth, Peter E Kammerer, Melinda Bal-
794 ansay, Rema Raman, Suzanne P Lindsay, and Gary T Brice. Epidemiology
795 of pathogen-specific respiratory infections among three US populations. *PLoS
796 One*, 9(12):e114871, 2014.
- 797 [20] Guojian Lv, Limei Shi, Yi Liu, Xuecheng Sun, and Kai Mu. Epidemiological
798 characteristics of common respiratory pathogens in children. *Scientific Reports*,
799 14(1):16299, 2024.
- 800 [21] Saverio Caini, Adam Meijer, Marta C Nunes, Laetitia Henaff, Malaika Zounon,
801 Bronke Boudewijns, Marco Del Riccio, and John Paget. Probable extinction of
802 influenza b/yamagata and its public health implications: a systematic literature
803 review and assessment of global surveillance databases. *The Lancet Microbe*,
804 2024.

- 805 [22] Zhiyuan Chen, Joseph L-H Tsui, Bernardo Gutierrez, Simon Busch Moreno,
806 Louis du Plessis, Xiaowei Deng, Jun Cai, Sumali Bajaj, Marc A Suchard,
807 Oliver G Pybus, et al. COVID-19 pandemic interventions reshaped the global
808 dispersal of seasonal influenza viruses. *Science*, 386(6722):eadq3003, 2024.
- 809 [23] Bryan T Grenfell, Ottar N Bjørnstad, and Bärbel F Finkenstädt. Dynamics of
810 measles epidemics: scaling noise, determinism, and predictability with the TSIR
811 model. *Ecological monographs*, 72(2):185–202, 2002.
- 812 [24] Samit Bhattacharyya, Per H Gesteland, Kent Korgenski, Ottar N Bjørnstad,
813 and Frederick R Adler. Cross-immunity between strains explains the dynamical
814 pattern of paramyxoviruses. *Proceedings of the National Academy of Sciences*,
815 112(43):13396–13400, 2015.
- 816 [25] Virginia E Pitzer, Cécile Viboud, Wladimir J Alonso, Tanya Wilcox, C Jessica
817 Metcalf, Claudia A Steiner, Amber K Haynes, and Bryan T Grenfell. Environmental
818 drivers of the spatiotemporal dynamics of respiratory syncytial virus in
819 the United States. *PLoS pathogens*, 11(1):e1004591, 2015.
- 820 [26] Katharine R Dean, Fabienne Krauer, Lars Walløe, Ole Christian Lingjærde, Barbara
821 Bramanti, Nils Chr Stenseth, and Boris V Schmid. Human ectoparasites
822 and the spread of plague in Europe during the Second Pandemic. *Proceedings
823 of the National Academy of Sciences*, 115(6):1304–1309, 2018.
- 824 [27] Margarita Pons-Salort and Nicholas C Grassly. Serotype-specific immunity
825 explains the incidence of diseases caused by human enteroviruses. *Science*,
826 361(6404):800–803, 2018.
- 827 [28] Sarah Cobey and Edward B Baskerville. Limits to causal inference with state-
828 space reconstruction for infectious disease. *PloS one*, 11(12):e0169050, 2016.
- 829 [29] Public Health Agency of Canada. Respiratory virus detections in
830 Canada. 2024. <https://www.canada.ca/en/public-health/services/surveillance/respiratory-virus-detections-canada.html>. Accessed Sep
831 4, 2024.
- 832 [30] Centre for Health Protection. Detection of pathogens from respiratory specimens.
833 2024. <https://www.chp.gov.hk/en/statistics/data/10/641/642/2274.html>. Accessed Nov 20, 2024.
- 834 [31] Centre for Health Protection. Detection of gastroenteritis viruses from faecal
835 specimens. 2024. <https://www.chp.gov.hk/en/statistics/data/10/641/717/3957.html>. Accessed Nov 20, 2024.
- 836 [32] Korea Disease Control and Prevention Agency. Acute respiratory infection,
837 Sentinel surveillance infectious diseases. 2024. <https://dportal.kdca.go.kr/pot/is/st/ari.do>. Accessed Nov 20, 2024.
- 838

- 842 [33] Edward Goldstein, Sarah Cobey, Saki Takahashi, Joel C Miller, and Marc Lip-
843 sitch. Predicting the epidemic sizes of influenza A/H1N1, A/H3N2, and B: a
844 statistical method. *PLoS medicine*, 8(7):e1001051, 2011.
- 845 [34] Bob Carpenter, Andrew Gelman, Matthew D Hoffman, Daniel Lee, Ben
846 Goodrich, Michael Betancourt, Marcus A Brubaker, Jiqiang Guo, Peter Li,
847 and Allen Riddell. Stan: A probabilistic programming language. *Journal of*
848 *statistical software*, 76, 2017.
- 849 [35] Stan Development Team. RStan: the R interface to Stan, 2024. R package
850 version 2.32.6.